

Jones et al., 2013). *GSP-Spec* is composed of three research groups having different and complementary expertises in automated stellar classification from spectral data. In this article, we present the parametrization performed within this working group for RVS spectra.

The RVS is a high-resolution integral-field spectrograph that will survey the whole sky at a rate of about 100 spectra per second, producing about 15 billion of spectra during the mission. From its preliminary real performances, the RVS will collect spectra with large enough signal-to-noise ratio (S/N) in order to derive their radial velocity for stars brighter than $G_{\text{RVS}} \lesssim 16$ (i.e. about 150 million stars, G_{RVS} being the *Gaia* magnitude of the targets through the RVS filter). This limiting magnitude corresponds to $V \lesssim 17.3$ for a solar-type star (for the corresponding magnitudes in other photometric *Gaia* bands, see Tab. 2 and Fig. 4 presented in Sect.3.2). Several tens of millions of stars will be observed by the RVS down to a magnitude of $G_{\text{RVS}} \lesssim 13$, and about 5 million stars down to $G_{\text{RVS}} \lesssim 12$.

The RVS will provide spectra in the CaII IR triplet region (from 847 to 871 nm²) at a spectral resolution of $\sim 11\,200^3$. In addition to the CaII strong lines, one encounters, in the RVS spectral range and for late-type star spectra, weak lines of Si I, Ti I, Fe I, etc. In hotter (A-F types) star spectra, weak lines of N I, S I, and Si I appear around the Ca II lines and the strong Paschen hydrogen lines (see Fig. 1 & 2). Even hotter ($T_{\text{eff}} \gtrsim 15\,000$ K) stellar spectra contain lines of N I, Al II, Ne I, and Fe II whereas the Ca II lines start to decrease, and some He I lines appear.

On the other hand, the *Gaia* commissioning phase has revealed that the RVS suffers from (i) a level of scattered light higher than expected, and variable with time and CCD position (mainly sunlight scattered around sunshields) and thus an increased noise for part of the spectra, together with (ii) a time-variable throughput loss due to mirror contamination that reduces the collected signal by a few tenths of a magnitude. This last issue is regularly corrected thanks to de-contamination campaigns that reduce the loss to acceptable levels. Moreover, the *Gaia* DPAC has put in place a new version of the on-board software which results in a data collection scheme which is more robust against the stray light. This is mainly realised by lowering the auto-collimation width of read-out windows in the RVS (and possibly the astrometric field) such that less noise due to stray light is accumulated. The new video processing unit software that makes this possible has already been uploaded to the satellite (Fleitas et al., 2015). In addition, following the actual RVS performances revealed by the commissioning phase, it has also been decided that every RVS spectra will be provided in the nominal high-resolution mode to minimize the background contamination that is a function of the window width. Initially, a binning by a factor three for stars fainter than $G_{\text{RVS}} < 10$ was planned (e.g. Bailer-Jones et al., 2013), decreasing the effective resolution to around 7500. This possibility has now been definitively abandoned.

In this paper, the above mentioned post-launch RVS characteristics are taken into account and the new S/N-magnitude relation recently published by the European Space Agency has been adopted⁴. In addition, the expected final *GSP-Spec* performances are given for the actual RVS resolution of $\sim 11\,200$. Nevertheless,

the influence of the effective resolution change, at a constant S/N value, is studied in Sect. 3.4.

The main goal of the RVS is to measure the radial velocity of the stars in order to get their full 3D space motions when combined with the *Gaia* proper motions. However, the RVS data will be also very useful to parametrize brighter stars observed by *Gaia* in complement to the parametrization performed independently from the two more sensitive low-resolution spectrophotometers (see Liu et al., 2012, for an estimate of the expected parametrization performances with BP/RP data together with the performance improvements presented in Bailer-Jones et al. (2013) and Andrae et al. (2015, in preparation)). We point out that, in the present work, we do not consider for *GSP-Spec* any (*a-priori*) input from the BP/RP parametrization although this is one of the alternatives implemented in the *Gaia* global data processing pipeline developed by CU8 and called Astrophysical parameters inference system (Apsis, see Bailer-Jones et al., 2013).

Since *Gaia* scans the whole sky, each target will be observed several tens of times depending on their location on the sky (with an average of 40 epochs per stars for the RVS at the end of the mission, assuming the nominal 5-year mission). As a consequence, the S/N of the combined spectra will increase with time during the mission and we will have to re-parametrize these better quality spectra delivered by the successive releases. In the following, we consider RVS end-of-mission spectra that are a combination of the successive individual observations. It is expected that any star brighter than $G_{\text{RVS}} \lesssim 14$ (i.e. several tens of millions) will be parametrized by *GSP-Spec*. The estimated stellar parameters will be the effective temperature (T_{eff}), the surface gravity ($\log(g)$), the global metallicity ($[M/H]$), and the abundance of α -elements versus iron ($[\alpha/Fe]$). In a second step and whenever possible (depending on spectral type, metallicity, S/N ratio, radial velocity shifts...), the individual chemical abundances of several species as Fe, Ca, Mg, Ti, and Si will be also measured. This should be performed for about five million sources with an expected accuracy of about 0.1 dex for $G_{\text{RVS}} \lesssim 12$ owing to a specific optimization method that is under development (Guiglion et al., 2014).

The amount of spectra to parametrize requires the use of automated methods that have to be fast enough and able to manage different types of stars. Therefore, *GSP-Spec* is currently composed of different independent codes based on different algorithms. The advantage of having different codes is to get independent parameter estimates and to get the best parameters all across the studied space (a given algorithm could provide excellent results for some parameter combinations and/or S/N ratios but rather poor results for others). Therefore, every RVS spectra will be parametrized by the different *GSP-Spec* codes and most stars will be assigned to several parameter estimates with quality flags.

In this paper, we describe the *GSP-Spec* codes and their expected performances for different types of stellar populations as they have been implemented at the *Gaia* launch epoch. Increasingly optimized versions of the *GSP-Spec* module of Apsis (see Bailer-Jones et al., 2013) are delivered at each operations cycle. *GSP-Spec* is expected to be running in operations cycle 4 in 2017, with a possible contribution from the third *Gaia* data release (planned around 2018).

In the following, we first present in Sect. 2 the codes specifically developed or adapted to the RVS stellar spectra by *GSP-Spec* in order to estimate their stellar atmospheric parameters together with their enrichment in α -elements with respect to iron. We then detail in Sect. 3 the methodology adopted for testing and comparing these different codes and their *GSP-Spec* perfor-

² The RVS red edge has been shifted from 874 to 871 nm with respect to the original configuration, following a change in the RVS filter effective transmission. In the present work, we have thus adopted this 871 nm cut-off for the simulated spectra.

³ The design specification of $R \sim 10\,500$ being exceeded.

⁴ See <http://www.cosmos.esa.int/web/gaia/sn-rvs>

mances on simulated spectra at different RVS magnitudes are investigated and discussed in Sect. 4. The end-of-mission *GSP-Spec* expected parametrization is described in Sect. 5 for different types of stars and S/N ratios. We then provide a comparison with the expected performances for the parametrization from BP/RP photometry (Sect. 6) and from some ground-based spectroscopic surveys (Sect. 7). We finally conclude this work in Sect. 8.

2. The *GSP-Spec* automated parametrization codes

In this work, four different codes for estimating the atmospheric stellar parameters and the overall $[\alpha/\text{Fe}]$ chemical index (the latter, for cool FGK-spectral type stars, only) have been tested for *GSP-Spec*: FERRE, GAUGUIN, MATISSE, and Artificial Neural Networks (ANN). These codes have already been extensively described in previous papers. We hereafter refer to the indicated references for their detailed description. We below provide only a brief summary of these codes and we mainly focus on the specificities that have been developed for *GSP-Spec*. Furthermore, we point out that most of these codes have already been separately used to parametrize real stellar spectra collected at a similar resolution and over the same wavelength region as the ones of the RVS (see references below). However, the present work is the first one to illustrate and compare their performances in the *Gaia* context.

Within the different data mining approaches that have been developed so far, *GSP-Spec* parametrization algorithms belong to the class using the mapping with reference models in a continuously variable space. In addition, they belong to the three main families of parametrization: optimization methods, projection methods and pattern recognition.

- The optimization codes (FERRE and GAUGUIN) perform a distance minimization between the full input spectrum and the reference spectra grid.

FERRE⁵ (Allende Prieto et al., 2006) is a FORTRAN90 code that compares the χ^2 between models and observations to identify the optimal set of atmospheric parameters (and/or abundances) of a star. The search is performed using the Nelder-Mead (1965) algorithm. The model evaluation is based on linear interpolation in a pre-computed grid, which is held on the computer's memory for speed. The observed and (interpolated) model spectra are forced to have the same mean value. Multiple searches are performed for each spectrum, initialized at 100 random positions in the grid. The code is parallelized over multiple cores using OpenMP and is made available upon request.

GAUGUIN (Bijaoui et al., 2012) is a classical local optimization method implementing a Gauss-Newton algorithm. It is based on a local linearisation around a given set of parameters that are associated to a reference synthetic spectrum (via linear interpolation of the derivatives). A few iterations are carried out through linearisation around the new solutions, until the algorithm converges towards the minimum distance. In practice, and in order to avoid trapping into secondary minima, GAUGUIN is initialized by parameters independently determined by other algorithms such as MATISSE (this is noted hereafter as MATISSE_G, see below). GAUGUIN is part of the analysis pipeline of the *Gaia* - ESO Survey (GES, Gilmore et al., 2012) for the GIRAFFE spectra (Recio-Blanco et al., 2015, in preparation).

⁵ The code is now public and available at: <http://hebe.as.utexas.edu/ferre>

- The MATISSE algorithm (Recio-Blanco et al., 2006) is a projection method in the sense that the full input spectra are projected into a set of vectors derived during a learning phase, based on the noise-free reference grids (see Sect. 3.1). These vectors are a linear combination of reference spectra and could be roughly viewed as the derivatives of these spectra with respect to the different stellar parameters. MATISSE is thus a local multi-linear regression method. Furthermore, a two-step procedure in the parameter estimation has been implemented within MATISSE to tackle non-linearity problems. Other recent applications of MATISSE to very large amounts of real observed spectra are the *AMBRE* project (de Laverny et al., 2013; Worley et al., 2012), the RAVE fourth Data Release (Kordopatis et al., 2013) and the *Gaia* - ESO Survey (see Recio-Blanco et al., 2015, in preparation).

- Finally, the ANN code uses a pattern recognition approach to parametrise the spectra.

The implementation of the ANN method for *GSP-Spec* has already been presented in Manteiga et al. (2010). Shortly, the architecture is a feed-forward network with three layers, trained with the online error back propagation algorithm. We generate one network for each stellar parameter where the number of neurons in the input layer coincides with the number of points of the format that was selected as signal representation. The output layer consists of the parameter to be predicted. The activation function for the hidden and output neurons of the network is a sigmoidal function. We also set the number of hidden neurons as the minimum between half the dimensionality of the input signal and 200 hidden units at maximum to reduce the computational burden of the training process. To deal with the initialization dependence and possible local minima, a series of training procedures are performed, until a near-optimal value is reached. On the other hand, early stopping is also used by means of a validation dataset to avoid the problem of over fitting, so that the network state which best generalizes is kept. Furthermore, to generalize the application to random spectra, we use 100 noised reference grid spectra during the training phase (see below). Finally, we made use of the wavelet decomposition to obtain new signal representations (low pass filter) which are used as the network inputs, both in the training and testing phases. In practice, this means that the results of this code are obtained by adopting the approximations of the first, second or third level in the wavelet pyramid (depending on the S/N value) as input for the ANN instead of the full spectra.

As outputs, these four codes provide the three atmospheric parameters (T_{eff} , $\log(g)$, and $[\text{M}/\text{H}]$) and the $[\alpha/\text{Fe}]$ chemical index (for FGK stars only) estimates together with their associated uncertainties (except for the ANN). For some of them (FERRE, GAUGUIN, MATISSE), a quality control parameter based on the goodness of the fit between the input spectrum and an interpolated one at the estimated parameters is also provided. We report in Tab.1 more details on some technical aspects of these codes.

3. Adopted methodology for quantifying the code performances

We present here the implemented homogeneous tests, including the used data and the analysis methodology, that estimate and compare the expected performances of the different *GSP-Spec* codes. The ultimate goal is to determine the optimal application fields of the different codes in terms of stellar types and S/N.

Table 1. Summary of technical aspects of the tested codes or algorithms.

| | Training phase | Programming language | Already implemented in Apsis |
|---------|----------------|----------------------|------------------------------|
| FERRE | No | Fortran | No |
| GAUGUIN | No | Fortran & Java | Yes |
| MATISSE | Yes | Fortran & Java | Yes |
| ANN | Yes | Java | No |

This will lead to the definition of the quality flags that will be assigned to the different parameter estimates within the *GSP-Spec* pipeline.

In this Section, the data used for the tests and the considered methodology for the analysis of the results are described. The different subsections present the steps of the followed procedure. In particular:

- The codes have been trained (when necessary, depending on the algorithm strategy, see Sect. 2) using large grids of noise-free RVS simulated synthetic spectra that are described in Sect. 3.1⁶
- Then, in order to perform an homogeneous comparison of the methods, parametrisation tests have been performed using noised random grids. The six adopted S/N values are 350, 150, 125, 40, 20 and 10. Those test grids contain interpolated spectra with arbitrary parameter values (see Sect. 3.2) that span the whole grid parameters range.
- A subsample of the previously noised random spectra, excluding non-physical parameter combinations and correctly populating the Hertzsprung-Russel diagram, has been selected (c.f. Sect. 3.3).
- Finally, we have tackled the problem of the recently abandoned RVS spectra rebin for stars with $G_{RVS} > 10$ (c.f. Sect. 3.4). The influence of this change in the *GSP-Spec* performances is quantified thanks to specific tests with one of the tested algorithms.

We would like to point out that, in this work, we favoured the use of synthetic spectra instead of real ground based observed ones (RVS data not being available yet) in order to explore any possible combination of the four parameters over a wide range of possible values and to keep a good homogeneity between the tests. We are fully aware that synthetic spectra may not be perfectly realistic when compared to observed stars for some parameter combinations but this will not affect the codes comparison. Of course, the application to real observed spectra will lead to larger errors (*external ones*) mostly due to the possible mismatches that could exist between synthetic and observed spectra. These effects will be quantified (and possibly corrected) during the mission owing to calibration with *reference stars* that will be (or already are for some of them) accurately parametrized (see Bailer-Jones et al., 2013).

Finally, we neglect in the following any effects that could be induced by wrong normalization or radial velocity corrections of the input spectra. Within the *Gaia* analysis pipeline, such problems will be examined, in collaboration with *GSP-Spec*, by the CU6 in charge of providing RVS spectra to CU8. The synthetic spectra described below are thus all at the rest frame and

⁶ We however point out that the non-trained codes also use the spectra grid for their parametrization based on a fitting process.

normalized. We, however, point out that, as the estimation of the atmospheric parameters and individual abundances can be quite sensitive to the pseudo-continuum normalization, an automated renormalization of the input spectra has already been implemented within *GSP-Spec*. Indeed, the RVS spectra can be renormalized through an iterative procedure coupled with the atmospheric parameters estimates. Such an iterative procedure has already be shown to be very successful when automatically applied to real spectra (Kordopatis et al., 2011; Worley et al., 2012; Kordopatis et al., 2013, and the GES pipeline, Recio-Blanco et al., 2015, in preparation). More specifically, we also point out that Kordopatis et al. (2011) have already shown that parametrization errors induced by normalization uncertainties as large as 3% of the continuum level for RVS-like spectra can be neglected if such an iterative renormalisation is implemented. This is however not considered in the following tests since we remind that we focus on already perfectly normalized input synthetic spectra.

3.1. Grids of reference spectra

The reference grids are a collection of noise-free high-resolution normalized synthetic spectra that have been computed from Kurucz model atmospheres. We favoured these Kurucz models, contrary to previous works based on MARCS model atmospheres (see, for instance, de Laverny et al., 2012), because they allow us to consider consistent spectra for cool FGK and hot BA-spectral type stars. The original computed spectra preserved the continuum slope, but then we continuum normalized each spectrum by (i) fitting iteratively a line and σ -clipping 10 times points that fell between 0.1σ and 3σ below and above the fit, respectively, and (ii) dividing the original spectrum by this final fit. We refer in the following to such *normalized* spectra, in which the slope in the spectrum, within the RVS wavelength domain, is not conserved. In practice, thanks to the estimates of stellar distance, and after accurate flux calibration, it would also be possible to analyse *Gaia* /RVS absolute flux spectra. This possibility is however not considered in this work.

Regarding the grid calculations, they were computed using Castelli & Kurucz (2003) model atmospheres and a line list from Kurucz⁷ enhanced with damping constants from Barklem et al. (2000) for atomic transitions. The calculations were done using the ASSET synthesis code (Koesterke et al., 2008; Koesterke, 2009), sampling the spectra with steps corresponding to 1 km/s. The values of the solar reference abundances in the synthesis are from Asplund et al. (2005), while those of the corresponding atmospheric structures are from Grevesse & Sauval (1998). The abundances of the α -elements were changed for the synthesis, but not in the model atmospheres.

Four parameters were considered for building the FGK-spectral type grid. These parameters are the effective temperature T_{eff} that varies from 4 000 to 8 000 K (with a step of 250 K), the surface gravity $\log(g)$ varying between 2.0 to 5.0 cm/s^2 (step of 0.5 dex), the mean metallicities varying from $10^{-2.5}$ to $10^{+0.5}$ the solar metallicity (with a step of 0.5 dex), and variations of ± 0.4 dex in the enrichment in the α -chemical species with respect to iron (step of 0.2 dex). This cool-star reference grid contains 5 831 spectra.

For hotter stars (from late B to F-spectral types), only the first three parameters were considered since the spectra become almost metal line-free with increasing T_{eff} . The effective temperature for this hot-star grid varies from 7 000 to 11 500 K (step of

⁷ from his website kurucz.harvard.edu

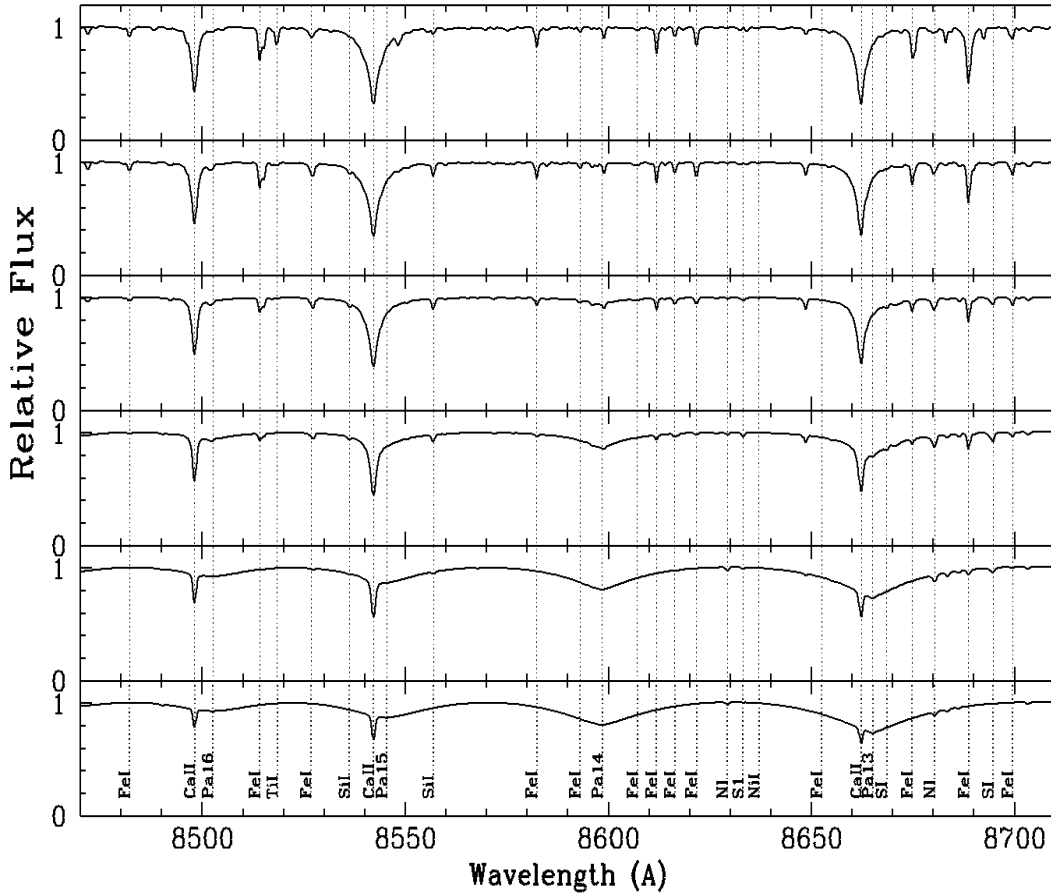


Fig. 1. Noise-free simulated RVS spectra for late B to K-spectral type metal-rich dwarf stars, included in the *reference* grids. The adopted effective temperatures are 11 000 K, 9 000 K, 7 500 K, 6 500 K, 5 500 K, and 4 500 K from bottom to top, respectively. The other stellar parameters are kept constant at $\log(g)=4.5$ cm/s^2 , $[M/H]=+0.0$ dex, and $[\alpha/Fe]=+0.0$ dex. The identified lines refer to most of the strongest atomic transitions that are present in the different spectra.

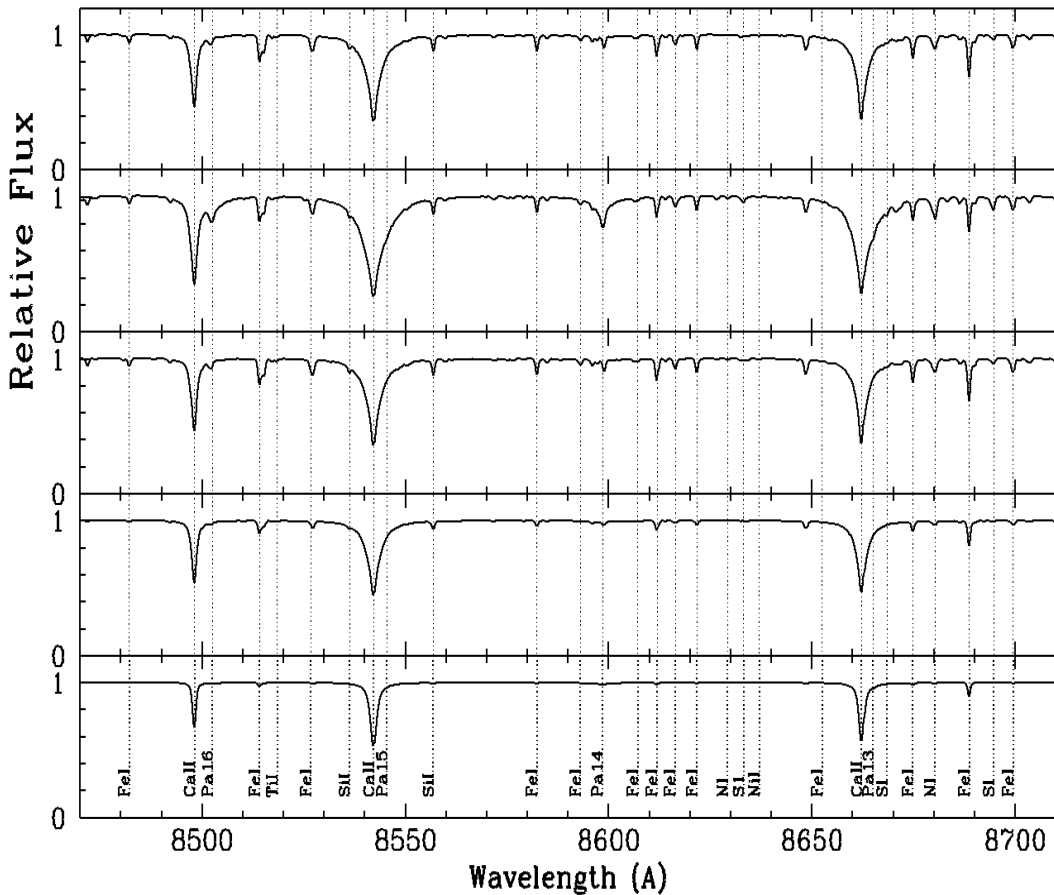


Fig. 2. Same as Fig. 1 but for cool stars only. Taking as reference a Solar spectrum defined with 5 750 K, $\log(g)=4.5$ cm/s^2 , $[M/H]=+0.0$ dex, $[\alpha/Fe]=+0.0$ dex and $R\sim 11\,000$ (top panel), the following panels show the effect of (from top to bottom): a change in surface gravity to $\log(g)=2.0$ cm/s^2 (second panel); and changes in the chemical composition (third, fourth and bottom panels showing respectively $[M/H]=+0.5$ dex and $[\alpha/Fe]=+0.2$ dex; $[M/H]=-1.0$ dex and $[\alpha/Fe]=+0.4$ dex; $[M/H]=-2.0$ dex and $[\alpha/Fe]=+0.4$ dex).

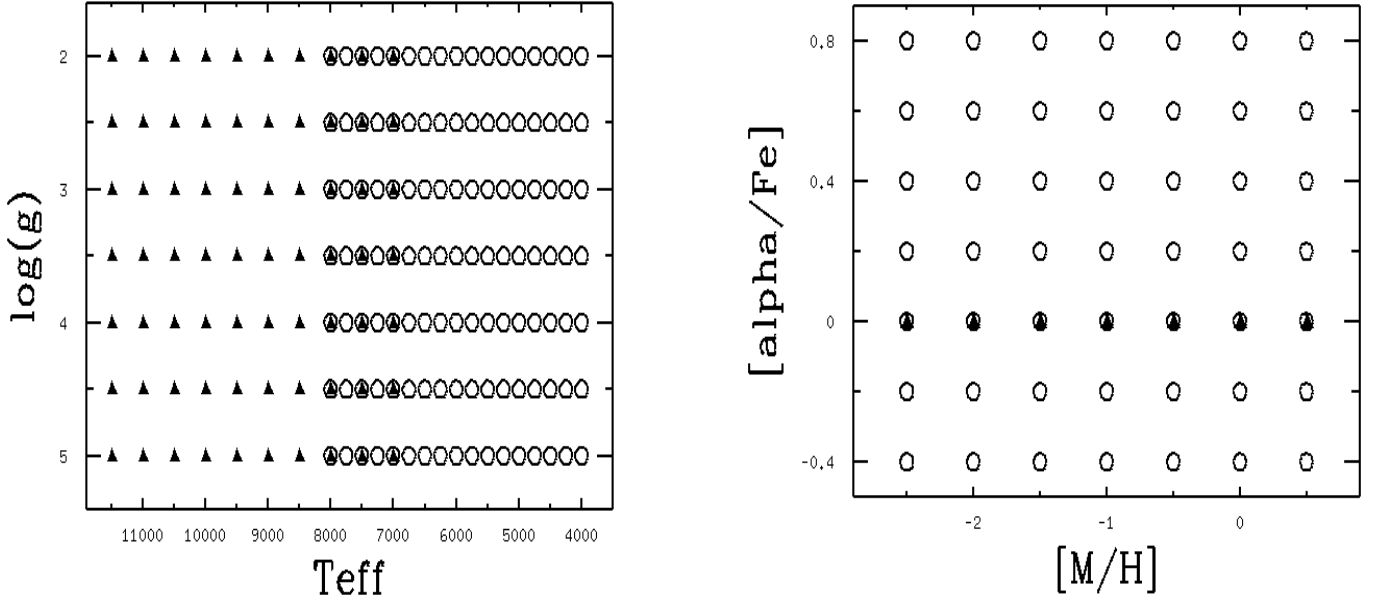


Fig. 3. Distribution of the *reference* synthetic spectra in the atmospheric parameter space (T_{eff} , $\log(g)$, $[M/H]$ and, $[\alpha/Fe]$ are in K, cm/s^2 , dex and dex, respectively). The cool-star and hot-star grids are shown with open circles and filled triangles, respectively. Any combination of the shown stellar parameters has been considered when building these grids, except for the hot-grid in which no variations in $[\alpha/Fe]$ have been considered (see filled triangles in the right panel).

500 K). The surface gravity and mean stellar metallicity ranges together with their variation steps are identical to those of the cool-star grid (without variations in $[\alpha/Fe]$). We end up with a reference grid of 490 hot stellar spectra.

We point out that any possible combination of the above mentioned stellar parameters has been considered to build these *square* cool and hot grids (i.e. without gaps in any of these three or four parameters).

In addition, these very high-resolution grids have then been degraded in order to mimic the RVS instrumental effects by convolution with a Gaussian profile for the spectral resolution ($R \sim 11\,200$) and adopting a sampling of ~ 0.024 nm/pixel (1 125 pixels in total). Additionally, a sampling of ~ 0.072 nm/pix (375 pixels) has been considered to produce two low resolution grids ($R \sim 7\,500$). They have been used to analyse the influence of the post-launch effective resolution change (c.f. Sect. 3.4).

In the following, we will refer to these two RVS synthetic spectra grids as the *reference* grids. For illustration, some spectra corresponding to the late B- to K-spectral types are shown in Fig. 1 together with the identification of some of their strongest lines. Moreover, Fig. 2 shows some cool stars spectra representative of different Galactic populations. Finally, the distribution of the atmospheric parameters and the $[\alpha/Fe]$ chemical index of the reference grids is shown in Fig. 3.

3.2. Grid of noised random spectra

From the *reference* high-resolution ($R \sim 11\,200$) and low-resolution ($R \sim 7\,500$) noise-free grids described above, interpolated noised synthetic spectra have been generated for the codes tests.

The interpolations were performed at random combinations of the four parameters. The S/N has then been simulated by adding noise (see below) to these interpolated spectra. The six adopted S/N values are 350, 150, 125, 40, 20 and 10. They correspond to the RVS filter magnitudes G_{RVS} values equal to 8.4, 10,

10.3, 11.8, 12.6, 13.4 according to the most recent RVS performances, including post-launch studied instrumental effects like straylight contamination, actual line spread function profiles, effects of window decentering and light loss.

We again point out that this added noise will allow us to estimate the parameter uncertainties caused by internal and instrumental errors and not the external errors, mainly dominated by possible synthetic spectra mismatches. Moreover, we report in Tab. 2 the magnitudes in the G and V -bands corresponding to $G_{\text{RVS}} = 13.5$ for different stellar types and in Fig. 4 the $(G-G_{\text{RVS}})$ versus $(V-G)$ relation for the range of T_{eff} studied in the present work. These estimated V , G and G_{RVS} -magnitudes and associated colours are based on the colour transformations provided by Jordi et al. (2010) together with the photometric colours – T_{eff} relations of Ramírez & Meléndez (2005) and Boyajian et al. (2012) for cool and hot stars, respectively.

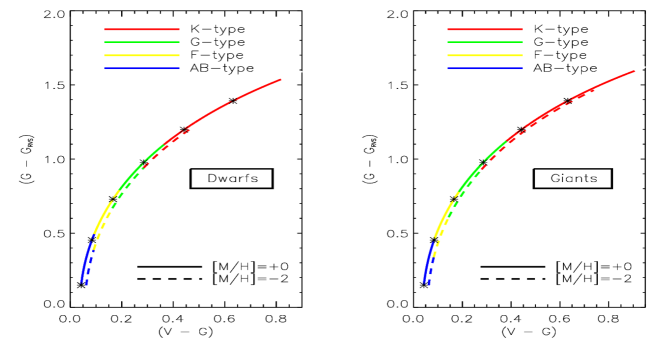


Fig. 4. $(G-G_{\text{RVS}})$ versus $(V-G)$ relation for the stellar types (colour-coded) defined in Sect. 5. For clarity reasons, the dotted lines (metal-poor stars) have been slightly ($+0.02$) horizontally shifted and the dwarf and giant regimes separated. The $(G-G_{\text{RVS}})$ and $(V-G)$ indexes only vary with the $(B-V)$ colour index but the covered ranges in both axis are dependent on the metallicity. The crosses along the curves refer to $(B-V)$ varying from 0.0 to 1.5 (step of 0.25) from bottom to top.

Table 2. V and G -magnitudes corresponding to $G_{\text{RVS}} = 13.5$ for some stellar types as defined in Sect. 5.

| Stellar type | V (mag) | G (mag) |
|--------------------|-----------|-----------|
| B dwarf | 13.69 | 13.65 |
| A dwarf | 13.83 | 13.77 |
| F metal-poor dwarf | 14.25 | 14.12 |
| F metal-rich dwarf | 14.32 | 14.18 |
| G metal-poor dwarf | 14.54 | 14.33 |
| G metal-rich dwarf | 14.76 | 14.48 |
| K metal-poor dwarf | 15.06 | 14.66 |
| K metal-rich dwarf | 15.37 | 14.82 |
| G metal-poor giant | 14.54 | 14.33 |
| G metal-rich giant | 14.76 | 14.48 |
| K metal-poor giant | 15.14 | 14.70 |
| K metal-rich giant | 15.52 | 14.89 |

Practically speaking, we have simulated end-of-mission RVS spectra based on the instrument performance information available to us. The CCD windows for the spectra, and therefore their noise properties depend mainly on the source brightness. On the other hand, we take into account that the binning in the spectral direction corresponds to one RVS pixel⁸

The average signal per binned pixel in one RVS spectrum I (single visit and single CCD) is approximately defined by the brightness in that band as $G_{\text{RVS}} = -2.5 \cdot \log(I \times q) + 22.5866$ where q , the number of binned pixels, is equal to 1260 for the high resolution and $q=420$ for the low one. We account for Poisson shot noise in the data, and the CCD readout noise, assumed to be 4 e-. Since the final RVS spectra will be accumulated from a variable number of visits, depending mainly on the location of a source on the sky, and since typically objects cross three CCDs per visit, we simulate individual observations (spectra acquired per CCD per visit), and then combine them to produce an end-of-mission spectrum for each source.

The final high and low resolution noised grids contain 20 000 random spectra at each selected G_{RVS} magnitude. They cover a wide range of atmospheric parameter values, including some non-physical combinations (unreal stars). Actually, 10 000 random spectra have been interpolated in each high/low resolution and cool/hot *reference* grids, having stellar parameters independent from the G_{RVS} values. Moreover, other additionally 100 random noised spectra were selected to train independently the ANN code (see Sect. 2). These grids are made available in FITS format upon request to the authors.

3.3. Final definition of noised random spectra samples

For the determination of the code performances, we selected a subsample of the previously described 20 000 random spectra, based on the following criteria:

- In order to correctly populate the Hertzsprung-Russell diagram (in terms of stellar parameters combinations, and not

⁸ Note that the RVS CCDs, as well as the other *Gaia* instruments, are operated in TDI mode, and hence talking about pixels (or *sample* as often used in *Gaia* literature) is not accurate, since the signal in any sample of a spectrum has been accumulated over many pixels as the star crosses the focal plane, but we will use this term for analogy.

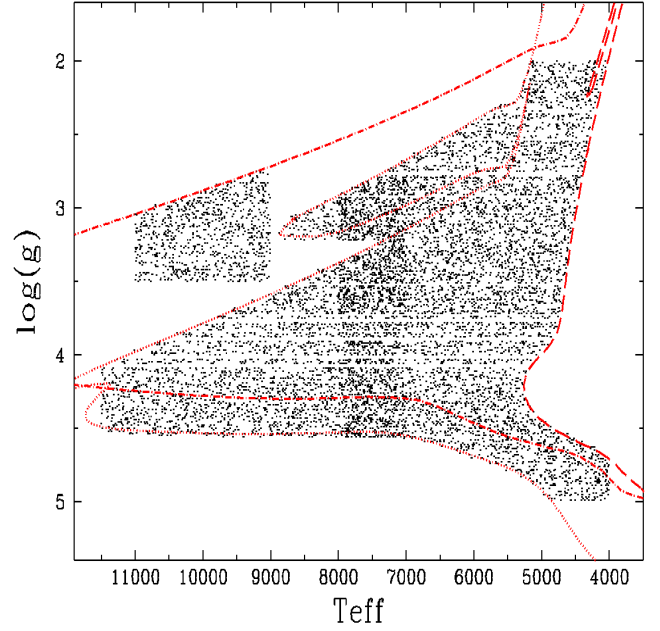


Fig. 5. Hertzsprung-Russell diagram of the random spectra (black dots) produced for the code performance tests (T_{eff} and $\log(g)$ are in K and cm/s^2 , respectively). The isochrones in long-dashed, dotted, and dash-dotted lines correspond, respectively to $Z=0.06$ and 13 Gyr, $Z=10^{-4}$ and 1 Gyr, and $Z=0.019$ and 100 Myr. The higher density of *random* spectra between 7 000 and 8 000 K is a consequence of the temperature overlap between the two different *reference* grids, for hot and cool stars (see Sect. 3.1), from which the random spectra have been interpolated.

of stellar lifetimes) as expected for a galaxy like the Milky Way with different stellar populations (assuming a standard initial mass function over a long period of star formation), we first retrieved PARSEC v1.1 isochrones from Bressan et al. (2012). The selected isochrones correspond to ages of 1 and 13 Gyr and metal content $Z = 10^{-4}$ and 0.06 (i.e. $[M/H] = -2.2$ and $+0.7$ dex).

- We then selected among the 20 000 interpolated spectra described in Sect. 3.2, those having a $(T_{\text{eff}}, \log(g))$ combination located between these two isochrones.
- Finally, for any selected $(T_{\text{eff}}, \log(g))$ combination, we chose all the available interpolated spectra (whatever their $[M/H]$ and $[\alpha/\text{Fe}]$ values are). These criteria led to the selection of 9 067 random spectra.
- In addition, and to consider the few hot giant stars that could be present in the RVS surveyed volume, we also retrieved an isochrone that is representative of younger stars (100 Myr) with solar metallicity ($Z = 0.19$). We then selected all the giants having (i) T_{eff} varying between 9 000 and 11 000 K and, (ii) a surface gravity comprised between 3.5 cm/s^2 and the isochrone gravity values. This procedure added 898 stars to the total selected sample.

The final high and low resolution *random* grids (as called hereafter) are composed of 9 965 noised random spectra at each of the six selected G_{RVS} or S/N-values. Their location in the Hertzsprung-Russell diagram is shown in Fig. 5. Their distribution in metallicity and α -enrichment is perfectly flat over the ranges $[-2.5, +0.5]$ and $[-0.4, +0.8]$, respectively, because of their random nature.

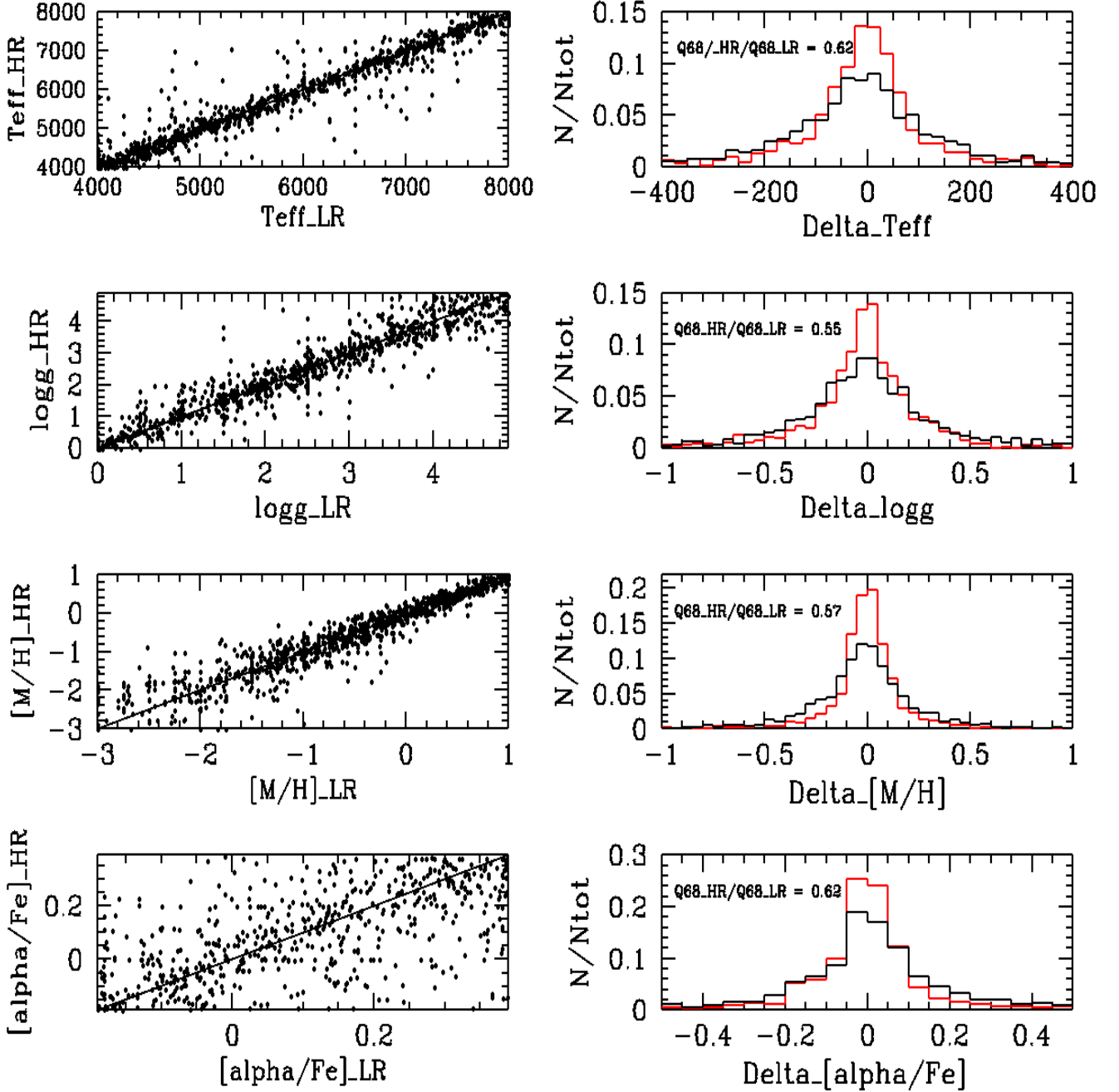


Fig. 6. Left panels: MATISSE_G results for cool random spectra of S/N~20 at the nominal high resolution (HR) compared to those for the lower resolution (LR) spectra of the same stars (and same S/N value). Right panels: normalized distribution of residuals for the high-resolution spectra (red curve) and for the low-resolution ones (black curve). The ratio of the 68% quantile values of both distributions is given for each stellar parameter.

3.4. Influence of the post-launch abandoned RVS spectra rebin on *GSP-Spec* performances

As explained in the Introduction, following the actual RVS performances revealed by the commissioning phase, it has been decided that every RVS spectra will be provided in the nominal high-resolution mode to minimize the background contamination. Before launch, a binning by a factor three for stars fainter than $G_{RVS} < 10$ was planned (e.g. Bailer-Jones et al., 2013), decreasing the effective resolution of their spectra to around 7500. The parametrization algorithms tested for *GSP-Spec* have there-

fore faced the problem of correctly evaluating this recent effective resolution change on their performances.

In this work, we have decided to analyse and to report the influence of this post-launch revision, while providing up-to-date performance expectations in agreement with the actual nominal RVS configuration. The resolution change issue has been tackled through the following steps:

- One of the codes, MATISSE_G (already integrated in the Apsis *Gaia* DPAC pipeline) was run both on all the noised random spectra with the nominal resolution of $R \sim 11\,200$, and on their corresponding rebinned spectra with effective

Table 3. Ratio of the 68% quantile values of the error distributions for nominal high resolution data and low effective resolution data (in the sense $Q68_{HR}$ divided by $Q68_{LR}$), as estimated with MATISSE_G. The results for different parameters and S/N values are presented.

| S/N | 125 | 40 | 20 | 10 |
|-----------------|------|------|------|------|
| G_{RVS} | 10.3 | 11.8 | 12.6 | 13.4 |
| T_{eff} | 0.62 | 0.66 | 0.62 | 0.62 |
| $\log(g)$ | 0.44 | 0.48 | 0.55 | 0.51 |
| [M/H] | 0.62 | 0.62 | 0.57 | 0.68 |
| [α /Fe] | 0.72 | 0.73 | 0.68 | 0.83 |

resolution $R \sim 7500$. The four left panels of Fig. 6 show the MATISSE_G results for cool random spectra of S/N \sim 20 at the nominal high resolution (HR) compared to those for the rebinned lower resolution (LR) spectra of the same stars and same S/N value. No particular trends are found between both solutions, justifying the possibility of correcting the parametrization performances for this rebinning change in the input data.

- The influence of the resolution in the parametrization precision was quantified by estimating the variation of the 68% quantile of the error (residuals) distributions (see also Sect. 4.2) due to the resolution change only. The four right panels of Fig. 6 present normalized distribution of residuals for the S/N \sim 20 high-resolution spectra results (red curve) and for the low-resolution ones (black curve) of cool random stars. The ratio of the 68% quantile values of both distributions is given for each stellar parameter. Similar ratios have been estimated for all the S/N values considered in this paper (c.f. Tab.3). In general, we can see that at constant S/N, the gain in the parameters precision when passing from the low resolution rebinned spectra to the nominal high resolution ones is of about one third.
- The results of the FERRE and ANN models which had been trained on rebinned low-resolution spectra for S/N 125, 40, 20 and 10 (fainter stars, as expected before launch), could now be rescaled to what we would expect if they had been trained on high-resolution spectra. The performances of those codes for the fainter stars, quantified through the 68% quantile of the residuals distribution, have been corrected by multiplying by the high-to-low resolution ratios derived in the previous step for each stellar parameter and each S/N value.

In summary, thanks to the above described synthetic spectra samples that consider the most up-to-date S/N-magnitude relation, and properly dealing with the actual RVS configuration and resolution, the parametrization tests presented here can be used to confidently estimate the future *GSP-Spec* performances.

4. Performance comparison of the different parametrization codes

We present in this section the performances of the tested methods for the sample of noised random FGK-type and BA-type stars defined in Sect. 3.3. In the following, the reported and discussed performances are those obtained by the FERRE and ANN codes together with those of MATISSE locally improved by GAUGUIN (noted MATISSE_G, hereafter). In particular, the

erosion of those codes performances as the information contained in the spectra decreases (ex. for increasing noise, lack of spectral signatures,...) is analysed here, in order to understand the behaviour of each method and its best applicability domain.

4.1. Distribution of residuals

To evaluate each code performances, we first computed the differences between the recovered (i.e. *estimated*) and real (*input*) atmospheric parameters, $\Delta\theta = \theta_{rec} - \theta_{real}$ with θ referring to T_{eff} , $\log(g)$, [M/H] and [α /Fe]. The $\Delta\theta$ will be referred as the *residuals*, hereafter.

Fig. 7 and Fig. 8 show the distribution of these $\Delta\theta$ residuals obtained with the three tested methods, for cool and hot stars random spectra, respectively. Both figures illustrate the results obtained at different G_{RVS} magnitudes ($G_{RVS} = 8.4, 10.3$ and 12.6 , that correspond to S/N values of 350, 125 and 20).

It can be seen that the residual distributions are always very peaked and depart from a perfect Gaussian-like distribution only at the faintest magnitudes (it has to be taken into account the fact that both figures are in logarithmic scale). Almost no outliers (spectra that are parametrized with an error well outside the main distribution) are seen. Moreover, these distributions are not biased at all except for the faintest hot star spectra where small biases appear only for some methods.

Moreover, we can notice that all the methods, at a given magnitude, recover the four atmospheric parameters with a rather similar quality. The performances are particularly excellent for the best-quality spectra ($G_{RVS} = 8.4$, this is also true as long as $G_{RVS} < 10$, see Fig.9 for instance). The residual distributions get wider as the noise increases, although the large majority of the spectra (see, for instance, the discussion on the $Q68_{\theta}$ below) are always recovered with an acceptable accuracy, even at $G_{RVS} = 12.6$. As expected, the parametrization in T_{eff} and [M/H] of the hottest faintest stars is of poorer quality since these spectra lack of sensitive spectroscopic signatures (see Fig. 1 where few atomic lines are seen, except the Ca II triplet, when $T_{eff} \gtrsim 8000$ K). However, the appearance of the broad Paschen lines still allows a very good estimate of the stellar surface gravity, even for very low quality spectra. In contrast, the surface gravity of the late-type stars is always the most difficult parameter to recover as already shown in several previous studies.

4.2. Quantification of method performances

To quantify each method performances, the 68% quantile of the $\Delta\theta$ distributions ($Q68_{\theta}$, hereafter) was adopted. This quantile could be viewed as the $1-\sigma$ error of the parameter recovery in case of a perfect Gaussian distribution of $\Delta\theta$. This is however not always the case, in particular, for low S/N ratios. Another statistical estimate of the performances is the systematic error (or bias) that corresponds to the mean of the differences between the recovered and real parameters ($\langle \Delta\theta \rangle$). In our case, the biases are almost always very small compared to the $Q68_{\theta}$ quantiles, for every method (see previous subsection). They can thus be neglected for our purpose and, as a consequence, they will not be discussed hereafter.

We first point out that we favoured, in the following, these $Q68$ quantiles over other possible statistical indicators (such as the root mean square, rms, or the Mean Absolute Residual, MAR) since we believe that the $Q68$ are more representative of the real performances (in terms of the bulk of the tested data) of the methods, particularly at low S/N ratios where the

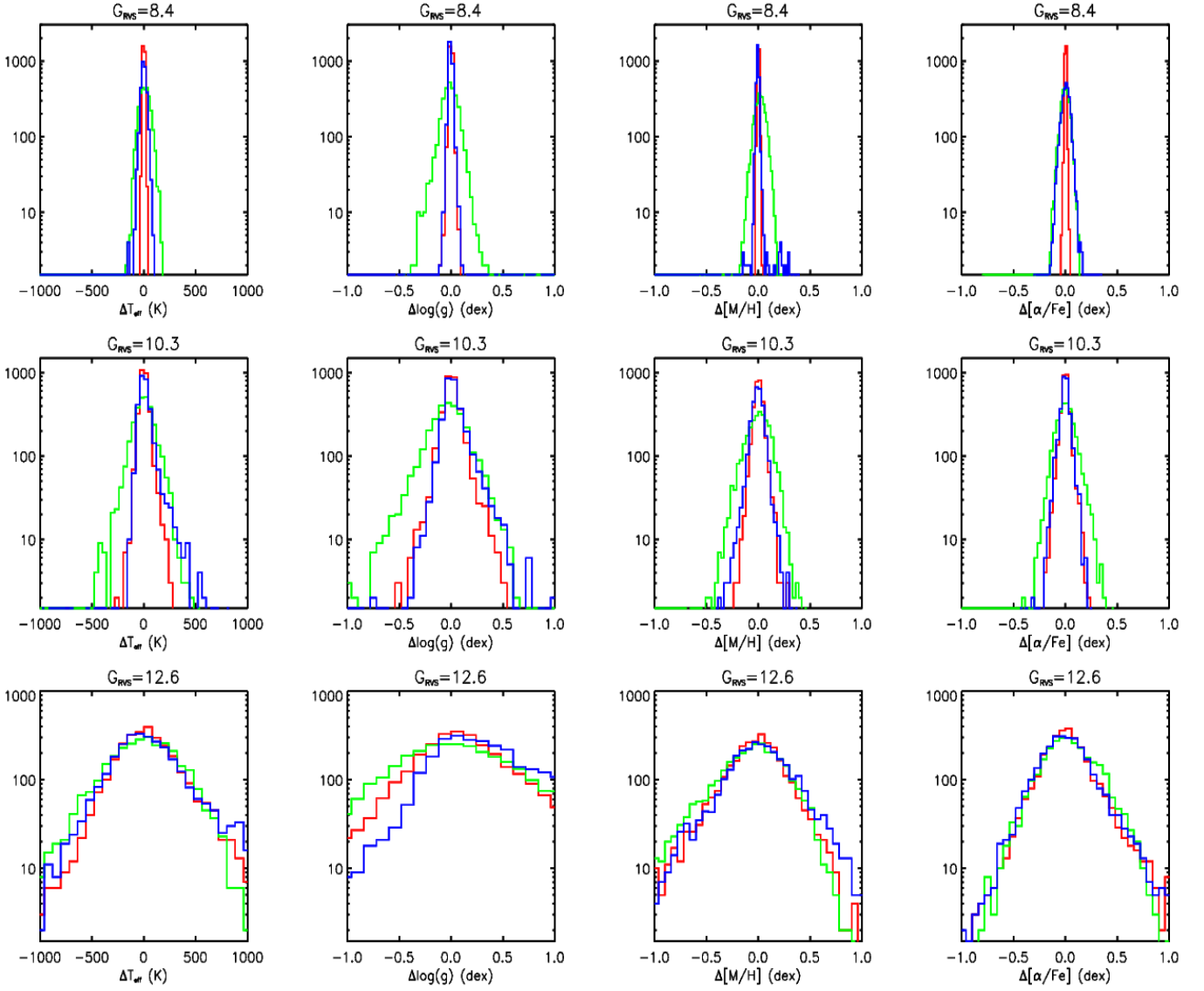


Fig. 7. Distributions of the residuals in the recovered atmospheric parameters ($\Delta\theta = \theta_{rec} - \theta_{real}$) for a subsample of cool random spectra with $G_{RVS} = 8.4, 10.3$ and 12.6 (i.e. S/N values of 350, 125 and 20), from top to bottom, respectively) and defined by $4000 < T_{eff} < 8000$ K. The different colours refer to the different tested methods: FERRE, ANN and, MATISSE_G in red, green and blue, respectively.

parametrization is more difficult to perform. As an illustration of this, we indeed compared (see Tab.4) the MAR_{θ} and rms_{θ} with the $Q68_{\theta}$ for all the random FGK-spectral type stars (about 6000 spectra) and three G_{RVS} magnitudes considered in the present article. In this table, the reported numbers are obtained with the FERRE code but our conclusions are independent of the adopted method. Although the MAR_{θ} and $Q68_{\theta}$ are very similar for the best quality spectra ($G_{RVS} < 10.3$), it can be seen that the MAR_{θ} are always smaller than the $Q68_{\theta}$ for every atmospheric parameter and that this departure increases for decreasing S/N. For instance, the MAR_{θ} gets close to the 60% quantiles when $G_{RVS} = 13.4$ (S/N=10). This results from the fact that, for fainter spectra, the $\Delta\theta$ distributions start to depart from a pure Gaussian distribution (see Fig. 7 & 8). In contrast, the rms_{θ} tend to correspond to higher quantiles than the $Q68_{\theta}$. As it is well known, this is caused by the high sensitivity of the rms to outliers. However, for the faintest magnitudes, these two statistical indicators become closer eachothers and the reported errors become in agreement.

4.2.1. General cool and hot random samples: noise and effective temperature effects

As a first step of the comparison, it is important to understand how the parametrization codes react to i) S/N degradation and ii) the general *palette* of spectral types (and therefore stellar effective temperatures) that the *GSP-Spec* module will have to deal with. To this purpose, Fig. 9 & 10 illustrate the degradation of each code performances with increasing noise for the late-type and early-type stars samples, respectively.

In addition, Fig. 11 and 12 show the scatter plots of the method-to-method results comparisons at $SNR \sim 125$ ($G_{RVS} \sim 10.3$) and $SNR \sim 20$ ($G_{RVS} \sim 12.6$) respectively. No important trends are found between the results of the different methods, confirming the consistency, with a higher or lower agreement, between the three types of results.

From the above mentioned plots, several conclusions can be derived:

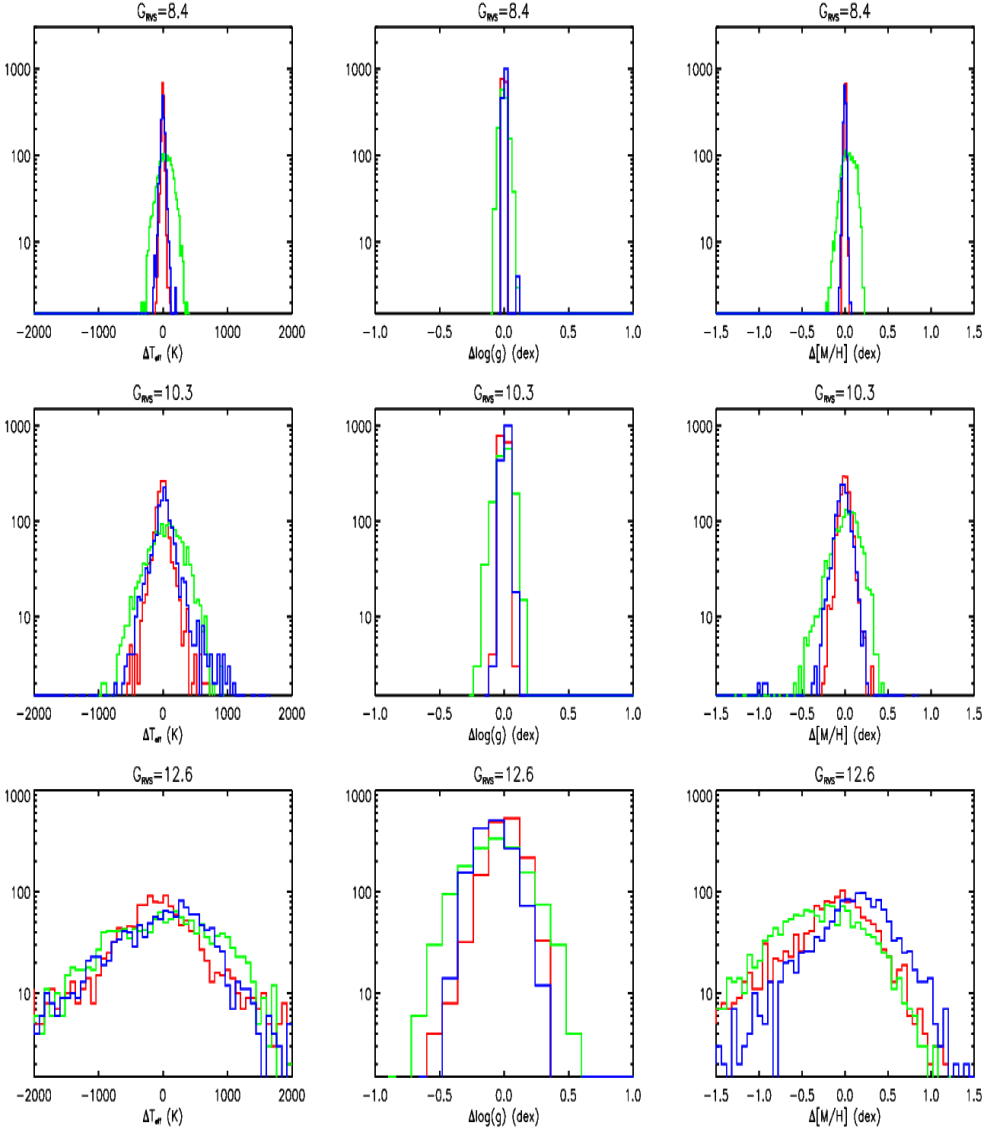


Fig. 8. Same as Fig. 7 but for a subsample of hot random spectra defined by $T_{\text{eff}} > 8000$ K.

Table 4. Comparison between the statistical performance indicators $Q68_\theta$, MAR_θ and rms_θ for the FERRE code. We report in the parenthesis of the last six columns the quantiles corresponding to the MAR_θ and the rms_θ .

| | $Q68_\theta$ | | | MAR_θ | | | rms_θ | | |
|----------------------------|--------------|-------|-------|--------------|-------------|-------------|--------------|-------------|-------------|
| S/N | 125 | 40 | 10 | 125 | 40 | 10 | 125 | 40 | 10 |
| G_{RVS} | 10.3 | 11.8 | 13.4 | 10.3 | 11.8 | 13.4 | 10.3 | 11.8 | 13.4 |
| T_{eff} (K) | 32.1 | 103.3 | 381.8 | 33.4 (Q69) | 101.4 (Q68) | 327.0 (Q62) | 56.1 (Q84) | 153.7 (Q80) | 436.0 (Q73) |
| $\log(g)$ (dex) | 0.05 | 0.15 | 0.49 | 0.05 (Q68) | 0.15 (Q67) | 0.40 (Q61) | 0.08 (Q82) | 0.22 (Q79) | 0.57 (Q71) |
| [M/H] (dex) | 0.05 | 0.14 | 0.36 | 0.05 (Q68) | 0.13 (Q65) | 0.29 (Q60) | 0.08 (Q82) | 0.18 (Q76) | 0.38 (Q71) |
| $[\alpha/\text{Fe}]$ (dex) | 0.04 | 0.14 | 0.35 | 0.04 (Q68) | 0.12 (Q66) | 0.27 (Q58) | 0.09 (Q83) | 0.18 (Q78) | 0.35 (Q68) |

- Most of the stars are well parametrized in T_{eff} , $\log(g)$ and [M/H] (together with $[\alpha/\text{Fe}]$ for the cool stars) by the three methods, working completely independently. This reinforces the idea that our estimates are robust.
- In the good to intermediate quality regime (for $G_{\text{RVS}} \lesssim 12.5$) and for cool and hot stars, two completely independent methods (FERRE and MATTISSE_G) produce very compatible results with no significant differences between both codes.

- In the low quality regime (for $G_{\text{RVS}} \gtrsim 12.5$) and cool stars, the three methods (FERRE, ANN and MATTISSE_G) give similar results (see also Fig. 7 bottom panel), although the ANN method seems to perform slightly better for very low S/N spectra ($G_{\text{RVS}} \sim 13.5$).
- For $G_{\text{RVS}} \gtrsim 12.5$ and hot stars, MATTISSE_G solutions seem slightly more robust.

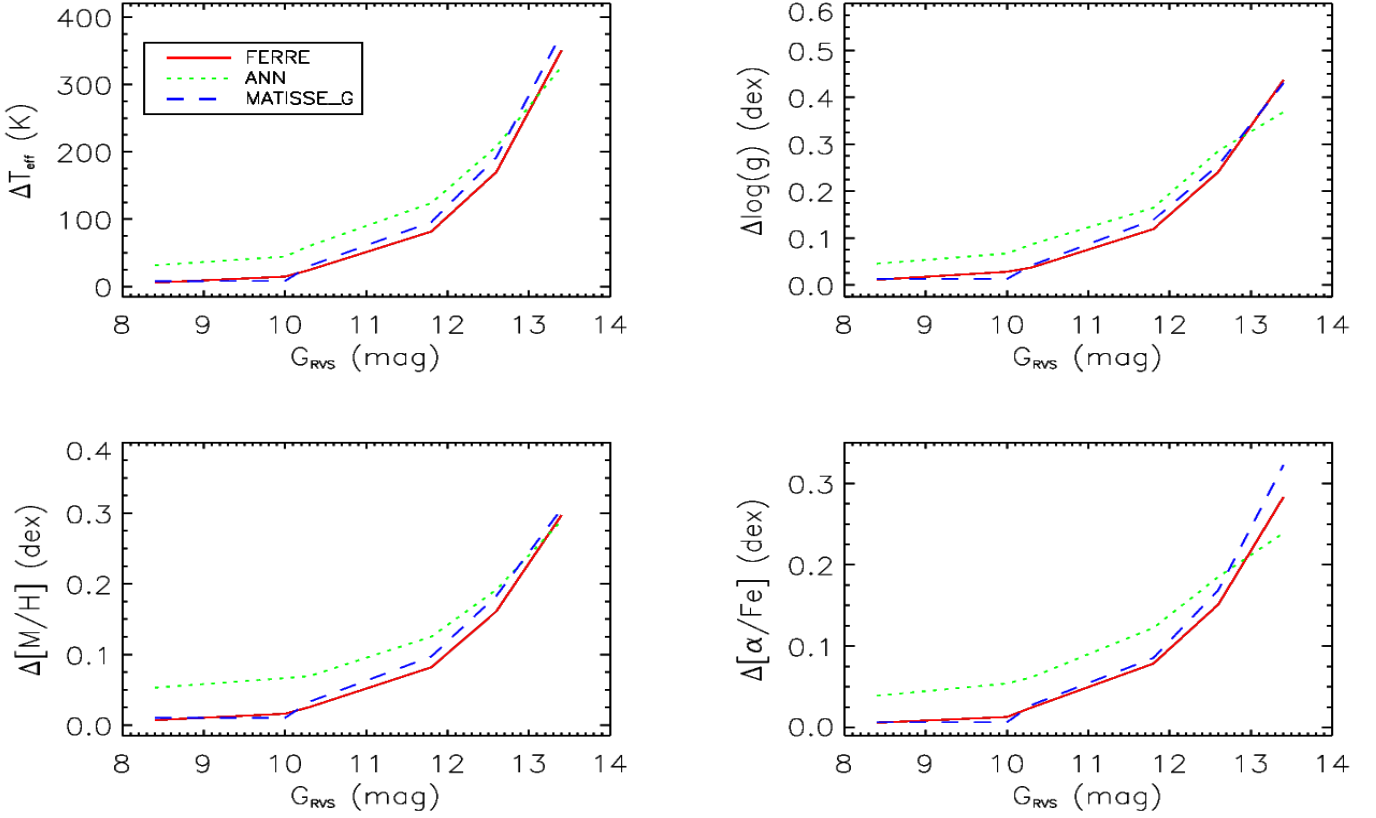


Fig. 9. Variation of the code performances (quantified by the 68% quantile) as a function of the magnitude, for the subsample of random cool stars defined by $4000 < T_{\text{eff}} < 8000$ K and $[M/H] \geq -1.0$ dex (2951 spectra in total).

4.2.2. Gravity and metallicity effects

To complete the robustness evaluation of the tested codes, and to understand their optimal applicability domains, we need to analyse their performances as a function of two additional parameters: stellar metallicity and surface gravity. To this purpose, we have chosen to illustrate two particular cases, concentrating on G and K-spectral type stars: rather metal-rich giants (Fig. 13) and dwarf stars with intermediate to low metallicities (Fig. 14). These two stellar types correspond to extreme cases of the *GSP-Spec* performances since (i) late-type giants are more easily parametrized than corresponding dwarfs and (ii) metal-rich star spectra exhibit much more spectral lines that ease their parametrization (see Sect. 5.1). The results show the following tendencies:

- In the good to intermediate quality regime (for $G_{\text{RVS}} \lesssim 12.5$), the FERRE and MATISSE_G codes are confirmed as the two methods providing the best results, independently of the metallicity and the gravity.
- In the low quality regime (for $G_{\text{RVS}} \gtrsim 12.5$) and for metal-rich stars, the three methods have similar performances, with ANN and MATISSE_G codes being slightly better for $\log(g)$.
- In the low quality regime (for $G_{\text{RVS}} \gtrsim 12.5$) and for metal poor stars, the ANN method is again providing the best results.

4.2.3. Summary of each code performances

In summary, from the above performance comparison, we can infer the following characteristics of each method application to the RVS data:

- The FERRE parametrization is always very satisfactory with good results for any parameters of any type of stars. However, for the faintest spectra, the performances degrade strongly leading to rather badly classified cool metal-poor dwarfs.
- The MATISSE_G method performs rather similarly to FERRE with satisfactory parametrization for every situation. MATISSE_G actually produces slightly better results when $G_{\text{RVS}} \lesssim 10.5$ but slightly worse for lower S/N ratios. In addition, MATISSE_G can sometimes produce the best estimates when the physical parameters information is low, although still not completely degraded at $G_{\text{RVS}} = 13.5$ (as for metal-rich cool giants and early-type stars).
- The ANN code always provides the best results for late-type stars when $G_{\text{RVS}} \approx 13.5$ (see Fig. 15). We stress that such stars will represent the largest sample collected by *Gaia* RVS. We point out that, however, for early-type stars, MATISSE_G sometimes performed better.
- It clearly seems that the present version of FERRE and MATISSE_G are very sensitive to the Gaussian-like dominated noise simulated in this work. This will be improved in the near future with the development of an optimized version of these codes when real RVS spectra will be available together with a precise knowledge of their noise properties. The adopted filtering for the ANN method will also have to be adapted in consequence.

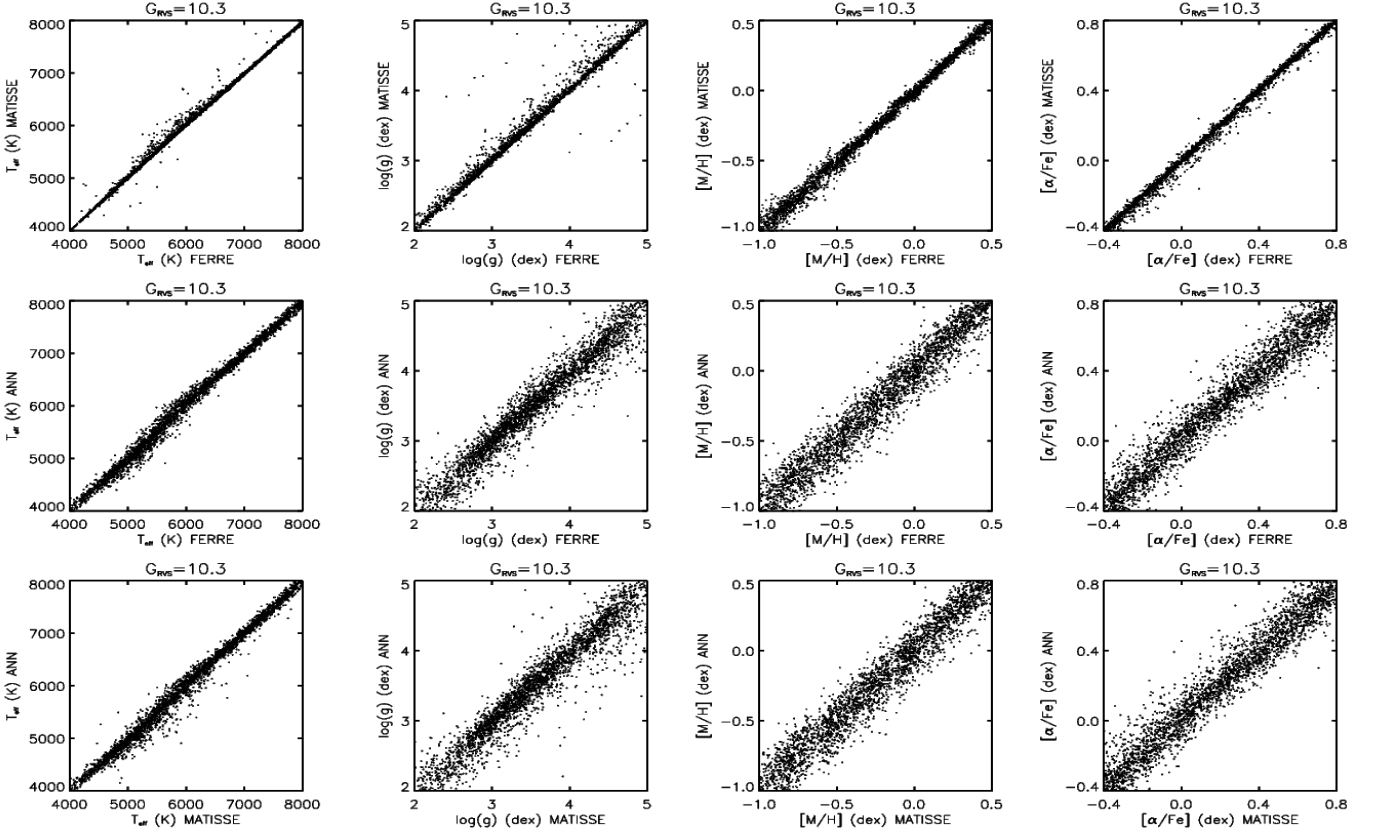


Fig. 11. Comparison of results method-to-method, at $\text{SNR} \sim 125$ ($G_{\text{RVS}} \sim 10.3$), for the subsample of random cool stars defined in Fig. 7.

5. Expected parametrization performances for *Gaia* RVS end-of-mission data

From the previous examination of the different parametrization codes, we have derived the final (end-of-mission) *GSP-Spec* expected results by choosing the optimal method for each applicability domain. We first point out that the same code solution was adopted for all four (or three for the early-type stars) atmospheric parameters, to avoid a mix of physically inconsistent parameters. This selection was performed through the following main rules, based on the conclusions of Sect. 4:

- For $G_{\text{RVS}} < 12.6$ ($S/N > 20$), the average of the FERRE and MATISSE_G solutions has been adopted as the final *GSP-Spec* performances since no significant differences appear between both methods.
- For $G_{\text{RVS}} \geq 12.6$ ($S/N \geq 20$) and FGK stars, the average of the FERRE, MATISSE_G and ANN is chosen for metal-rich and intermediate-metallicity stars, while the ANN method is favoured for late-type metal-poor spectra.
- $G_{\text{RVS}} \geq 12.6$ ($S/N \geq 20$) and hot stars, MATISSE_G solutions have been selected.

In any case, the *GSP-Spec* pipeline will also provide the individual results of the different codes in order to avoid any possible discontinuities between the different parameter and/or S/N regimes. Such discontinuities could be accidentally produced by these adopted rules. We however point out that this should be avoided owing to an accurate validation phase based on the analysis of benchmark stars (see an example of such a procedure within GES in Recio-Blanco et al., 2015, in preparation).

First of all, in order to describe the code performances for specific types of stars (in terms of spectral type, luminosity and

metallicity), we have defined different stellar classes characterized by the following atmospheric parameters ranges:

1. Metallicity ranges:
 - Metal-poor stars: $-2.25 \leq [M/H] < -1.25$ dex, roughly corresponding to Halo stars.
 - Intermediate-metallicity: $-1.25 \leq [M/H] < -0.5$ dex, typical of the Galactic thick disk
 - Metal-rich stars: $-0.5 \leq [M/H] \leq 0.25$ dex, roughly corresponding to the Galactic thin disc.
2. Gravity ranges:
 - Giant stars: $2.5 \leq \log(g) < 3.5$ cm/s²
 - Dwarf stars: $3.5 \leq \log(g) \leq 4.5$ cm/s²
3. Effective temperature ranges:
 - B-type stars: $10\,000 \leq T_{\text{eff}} \leq 11\,500$ K
 - A-type stars: $7\,500 \leq T_{\text{eff}} \leq 9\,500$ K
 - F-type stars: $6\,000 \leq T_{\text{eff}} \leq 7\,000$ K
 - G-type stars: $5\,000 \leq T_{\text{eff}} < 6\,000$ K
 - K-type stars: $4\,000 \leq T_{\text{eff}} < 5\,000$ K

This led to the 30 stellar classes (15 for dwarfs and 15 for cool giants)⁹. The end-of-mission *GSP-Spec* parametrization performances for these different classes and G_{RVS} magnitudes are presented in Tab. 5. The following subsections analyse and discuss the obtained results.

5.1. Performances for late-type stars

FGK-spectral type stars will represent the majority of the *Gaia* RVS targets and therefore, special attention has to be given

⁹ Some of these stellar classes correspond to rather infrequent real stars, particularly for the hot ones.

Table 5. Expected end-of-mission performances for *GSP-Spec* (quantified by the 68% quantile) for the different stellar classes defined in Sect. 5.

| | T_{eff} (K) | | | $\log(g)$ (dex) | | | [M/H] (dex) | | | [α /Fe] (dex) | | | | | | | | | |
|------------------------|----------------------|------|------|-----------------|------|------|-------------|------|------|-----------------------|------|------|------|------|------|------|------|------|--|
| S/N | 350 | 150 | 125 | 40 | 20 | 10 | 350 | 150 | 125 | 40 | 20 | 10 | 350 | 150 | 125 | 40 | 20 | 10 | |
| G_{RVS} (mag) | 8.4 | 10.0 | 10.3 | 11.8 | 12.6 | 13.4 | 8.4 | 10.0 | 10.3 | 11.8 | 12.6 | 13.4 | 8.4 | 10.0 | 10.3 | 11.8 | 12.6 | 13.4 | |
| DWARFS | | | | | | | | | | | | | | | | | | | |
| B metal-rich | 35 | 89 | 138 | 382 | 478 | 744 | 0.01 | 0.01 | 0.01 | 0.02 | 0.04 | 0.11 | 0.01 | 0.03 | 0.05 | 0.13 | 0.32 | 0.51 | |
| B intern. met. | 36 | 105 | 144 | 420 | 490 | 808 | 0.01 | 0.01 | 0.01 | 0.02 | 0.05 | 0.12 | 0.02 | 0.05 | 0.07 | 0.19 | 0.38 | 0.58 | |
| B metal-poor | 42 | 108 | 149 | 429 | 499 | 784 | 0.01 | 0.01 | 0.02 | 0.03 | 0.05 | 0.12 | 0.02 | 0.06 | 0.10 | 0.27 | 0.45 | 0.65 | |
| A metal-rich | 8 | 21 | 31 | 101 | 210 | 323 | 0.01 | 0.01 | 0.01 | 0.03 | 0.07 | 0.12 | 0.01 | 0.01 | 0.02 | 0.07 | 0.14 | 0.18 | |
| A intern. met. | 8 | 21 | 35 | 104 | 226 | 353 | 0.01 | 0.01 | 0.01 | 0.03 | 0.07 | 0.12 | 0.01 | 0.02 | 0.03 | 0.11 | 0.26 | 0.34 | |
| A metal-poor | 9 | 24 | 35 | 104 | 232 | 393 | 0.01 | 0.01 | 0.01 | 0.04 | 0.07 | 0.14 | 0.01 | 0.03 | 0.05 | 0.17 | 0.33 | 0.45 | |
| F metal-rich | 7 | 19 | 34 | 98 | 179 | 336 | 0.01 | 0.03 | 0.04 | 0.10 | 0.15 | 0.26 | 0.01 | 0.02 | 0.02 | 0.08 | 0.12 | 0.20 | |
| F intern. met. | 10 | 23 | 40 | 134 | 198 | 394 | 0.01 | 0.03 | 0.05 | 0.12 | 0.16 | 0.27 | 0.01 | 0.03 | 0.06 | 0.14 | 0.20 | 0.39 | |
| F metal-poor | 13 | 30 | 51 | 134 | 198 | 425 | 0.02 | 0.05 | 0.06 | 0.14 | 0.17 | 0.29 | 0.02 | 0.05 | 0.08 | 0.21 | 0.23 | 0.43 | |
| G metal-rich | 7 | 19 | 26 | 99 | 166 | 385 | 0.02 | 0.05 | 0.06 | 0.17 | 0.21 | 0.27 | 0.01 | 0.01 | 0.02 | 0.08 | 0.13 | 0.20 | |
| G intern. met. | 14 | 33 | 62 | 178 | 295 | 460 | 0.03 | 0.08 | 0.12 | 0.18 | 0.25 | 0.28 | 0.01 | 0.03 | 0.06 | 0.16 | 0.25 | 0.32 | |
| G metal-poor | 23 | 69 | 105 | 200 | 326 | 487 | 0.05 | 0.13 | 0.15 | 0.22 | 0.28 | 0.32 | 0.02 | 0.06 | 0.11 | 0.22 | 0.31 | 0.38 | |
| K metal-rich | 4 | 7 | 22 | 44 | 143 | 255 | 0.01 | 0.04 | 0.06 | 0.12 | 0.22 | 0.28 | 0.01 | 0.01 | 0.02 | 0.06 | 0.11 | 0.20 | |
| K intern. met. | 8 | 16 | 27 | 74 | 219 | 305 | 0.02 | 0.05 | 0.06 | 0.13 | 0.25 | 0.30 | 0.01 | 0.02 | 0.02 | 0.06 | 0.14 | 0.28 | |
| K metal-poor | 19 | 47 | 80 | 183 | 250 | 422 | 0.04 | 0.15 | 0.15 | 0.20 | 0.28 | 0.33 | 0.02 | 0.05 | 0.08 | 0.17 | 0.27 | 0.36 | |
| GIANTS | | | | | | | | | | | | | | | | | | | |
| B metal-rich | 11 | 31 | 32 | 107 | 365 | 450 | 0.01 | 0.01 | 0.01 | 0.04 | 0.06 | 0.12 | 0.01 | 0.02 | 0.03 | 0.12 | 0.28 | 0.38 | |
| B intern. met. | 13 | 32 | 45 | 139 | 390 | 473 | 0.01 | 0.01 | 0.01 | 0.04 | 0.06 | 0.12 | 0.01 | 0.03 | 0.06 | 0.19 | 0.40 | 0.45 | |
| B metal-poor | 16 | 33 | 52 | 194 | 411 | 493 | 0.01 | 0.01 | 0.01 | 0.04 | 0.06 | 0.12 | 0.02 | 0.05 | 0.09 | 0.27 | 0.43 | 0.48 | |
| A metal-rich | 7 | 27 | 33 | 97 | 209 | 369 | 0.01 | 0.01 | 0.01 | 0.04 | 0.07 | 0.12 | 0.01 | 0.02 | 0.02 | 0.07 | 0.13 | 0.17 | |
| A intern. met. | 9 | 27 | 34 | 102 | 229 | 382 | 0.01 | 0.01 | 0.01 | 0.04 | 0.07 | 0.14 | 0.01 | 0.02 | 0.04 | 0.12 | 0.22 | 0.30 | |
| A metal-poor | 11 | 27 | 36 | 110 | 235 | 403 | 0.01 | 0.01 | 0.01 | 0.04 | 0.08 | 0.14 | 0.01 | 0.04 | 0.04 | 0.17 | 0.31 | 0.43 | |
| F metal-rich | 5 | 10 | 18 | 63 | 134 | 253 | 0.01 | 0.02 | 0.03 | 0.08 | 0.16 | 0.22 | 0.01 | 0.01 | 0.02 | 0.06 | 0.13 | 0.16 | |
| F intern. met. | 6 | 16 | 22 | 69 | 147 | 265 | 0.01 | 0.03 | 0.03 | 0.11 | 0.17 | 0.22 | 0.01 | 0.03 | 0.04 | 0.11 | 0.17 | 0.22 | |
| F metal-poor | 6 | 17 | 24 | 71 | 148 | 280 | 0.01 | 0.04 | 0.04 | 0.11 | 0.18 | 0.32 | 0.02 | 0.05 | 0.09 | 0.21 | 0.20 | 0.24 | |
| G metal-rich | 5 | 12 | 22 | 92 | 177 | 350 | 0.01 | 0.03 | 0.04 | 0.15 | 0.22 | 0.36 | 0.01 | 0.01 | 0.02 | 0.08 | 0.14 | 0.16 | |
| G intern. met. | 10 | 26 | 47 | 166 | 254 | 373 | 0.02 | 0.06 | 0.10 | 0.21 | 0.30 | 0.44 | 0.01 | 0.03 | 0.05 | 0.16 | 0.23 | 0.25 | |
| G metal-poor | 15 | 43 | 54 | 170 | 265 | 383 | 0.04 | 0.11 | 0.12 | 0.24 | 0.34 | 0.44 | 0.02 | 0.06 | 0.07 | 0.18 | 0.27 | 0.31 | |
| K metal-rich | 5 | 11 | 21 | 64 | 147 | 237 | 0.02 | 0.04 | 0.06 | 0.17 | 0.29 | 0.43 | 0.01 | 0.01 | 0.02 | 0.06 | 0.12 | 0.17 | |
| K intern. met. | 6 | 18 | 29 | 91 | 211 | 333 | 0.02 | 0.06 | 0.08 | 0.21 | 0.33 | 0.50 | 0.01 | 0.02 | 0.03 | 0.11 | 0.19 | 0.28 | |
| K metal-poor | 13 | 39 | 65 | 200 | 289 | 444 | 0.04 | 0.10 | 0.13 | 0.28 | 0.34 | 0.52 | 0.02 | 0.05 | 0.07 | 0.19 | 0.25 | 0.31 | |

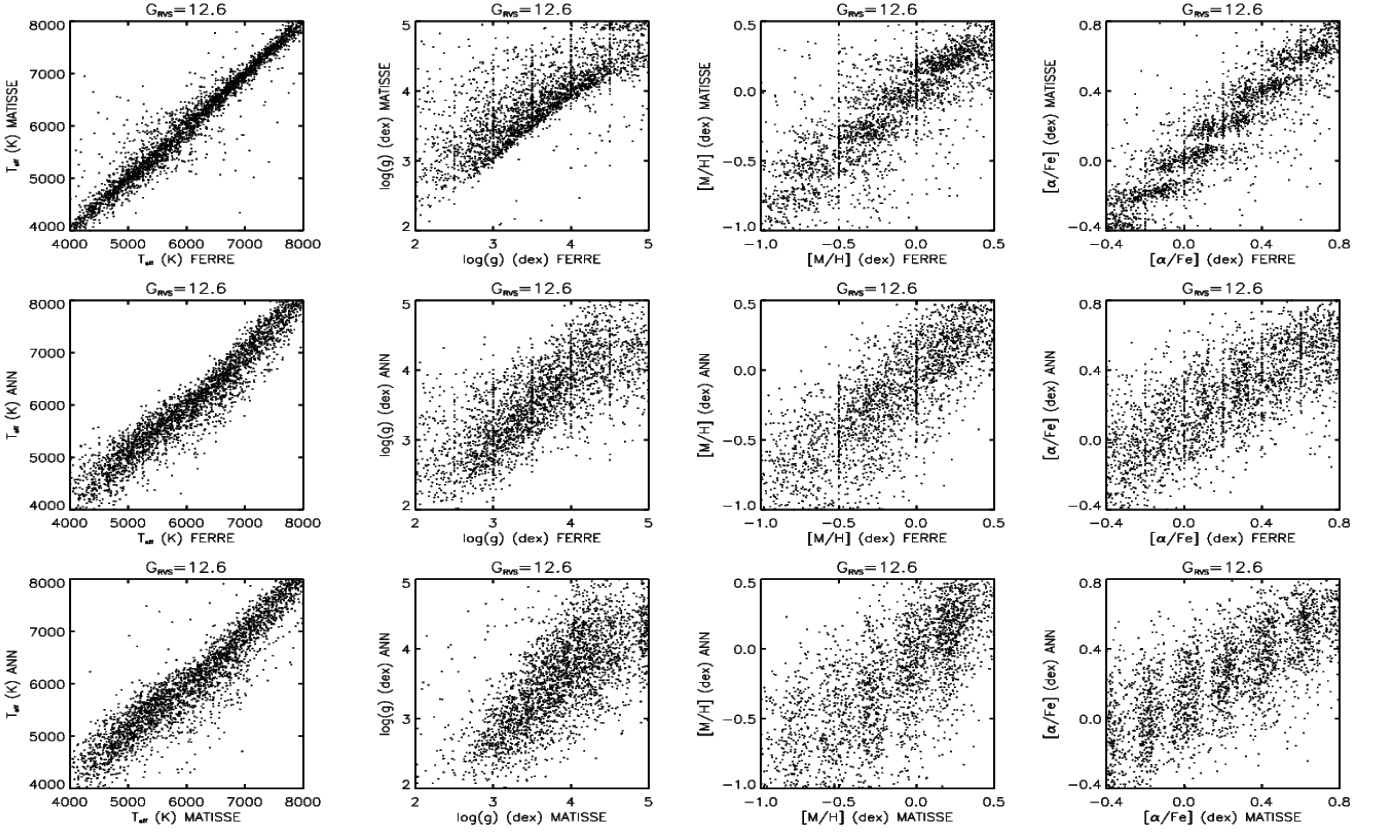


Fig. 12. Same as Fig. 11 but at SNR ~ 20 ($G_{\text{RVS}} \sim 12.6$).

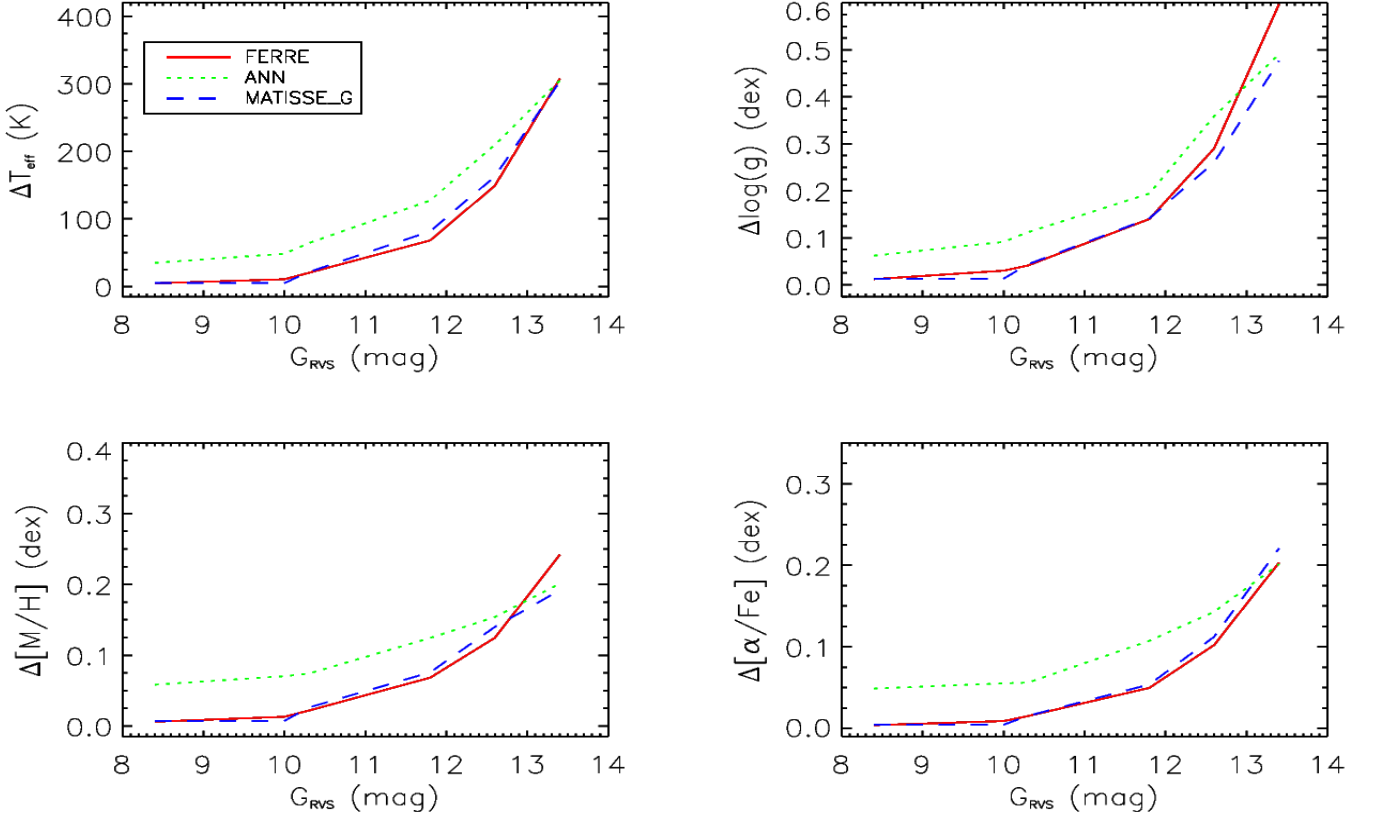


Fig. 13. Same as Fig. 9 but for a subsample of random cool giant stars defined by $T_{\text{eff}} < 6000$ K, $\log(g) < 3.5$ cm/s^2 and $[M/H] \geq -0.5$ dex (557 stars in total)

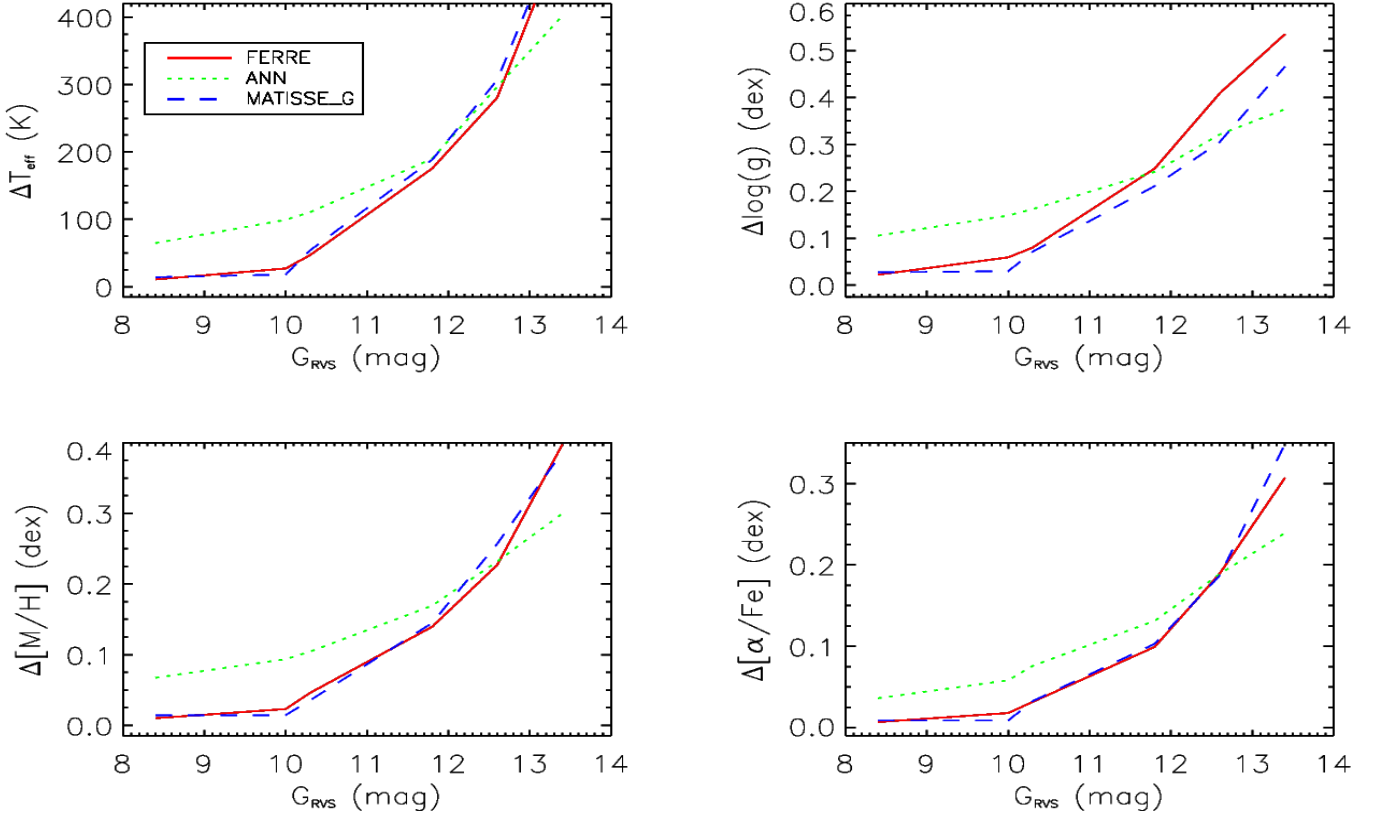


Fig. 14. Same as Fig. 9 but for a subsample of random cool dwarf stars defined by $T_{\text{eff}} < 6000$ K, $\log(g) \geq 3.5$ cm/s² and $-1.25 \leq [M/H] < -0.5$ dex (376 stars in total)

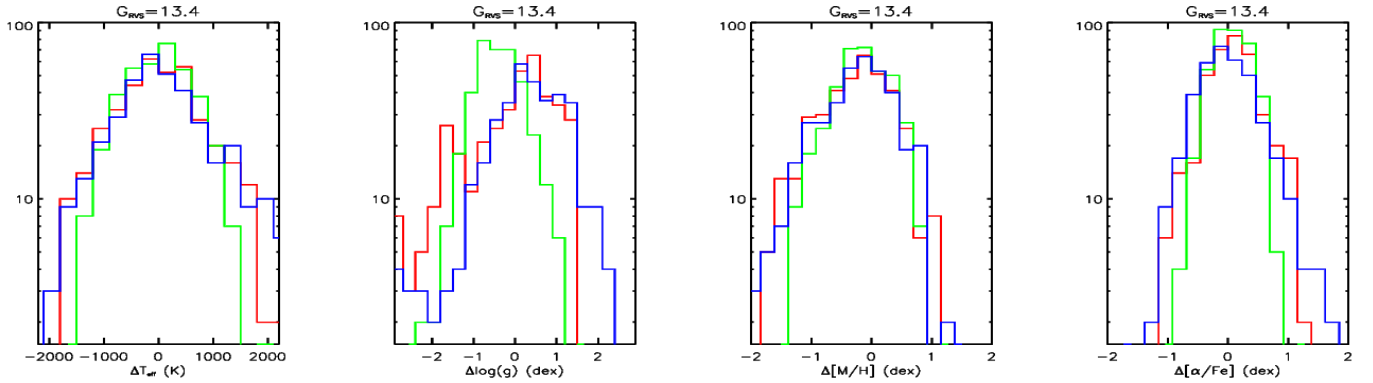


Fig. 15. Same as Fig. 7 but for the subsample of Fig. 14 and $G_{\text{RVS}} = 13.4$.

to the *GSP-Spec* parametrisation capabilities of their spectra. Figures 16 and 17 illustrate the expected errors (defined as the 68% quantile of the $\Delta\theta$ distributions, c.f. Sect. 4) for G-type dwarfs and K-type giants, respectively. The different curves on each panel correspond to the three metallicity intervals defined above and reported in Tab. 5.

For stars with $G_{\text{RVS}} \leq 12.5$, the FGK stars parametrisation is accurate enough to precisely characterize the stellar properties (typical errors are smaller than 0.1 dex in $[M/H]$ and $[\alpha/Fe]$) and, therefore, to conduct Galactic population studies as already performed from ground-based Galactic archaeology surveys (see Recio-Blanco et al., 2014, for instance). Such accuracy in the stellar atmospheric parameters will allow, in a second step, quite accurate determinations of individual chemical abundances (see, for instance, Guiglion et al., 2014). This is specially true for metal rich and intermediate metallicity stars, that will be the

most abundant ones in the magnitude volume sounded by the RVS. For the faintest stars at $G_{\text{RVS}} \geq 12.5 - 13.0$, where the noise amplitude becomes too strong with respect to the available stellar spectroscopic signatures, the accuracy in the parameters estimation degrades (with metallicity errors in the range 0.2 to 0.5 dex, for instance).

On the other hand, the dependency of the parameters accuracy on the stellar metallicity is illustrated by the clear separation of the continuous (metal-rich), dashed (metal-intermediate) and dotted (metal-poor) curves. As expected, metal-rich stars are more easily parametrized than the cool metal-poor ones whatever the S/N ratios are. This is evidently caused by the number of spectroscopic signatures (lines sensitive to the atmospheric parameters and abundances) available to perform the spectral analysis that dramatically decreases below $[M/H] \leq -0.5$ dex. This is also illustrated in Figures 18 and 19, showing the dependences of

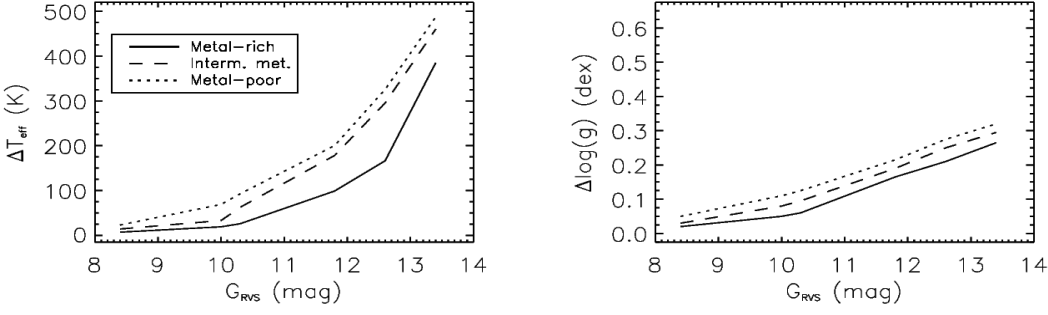


Fig. 16. Variation of the end-of-mission *GSP-Spec* performances (quantified by the 68% quantile of the residuals) as a function of increasing magnitudes for the G-dwarf stars defined in Sect. 5.

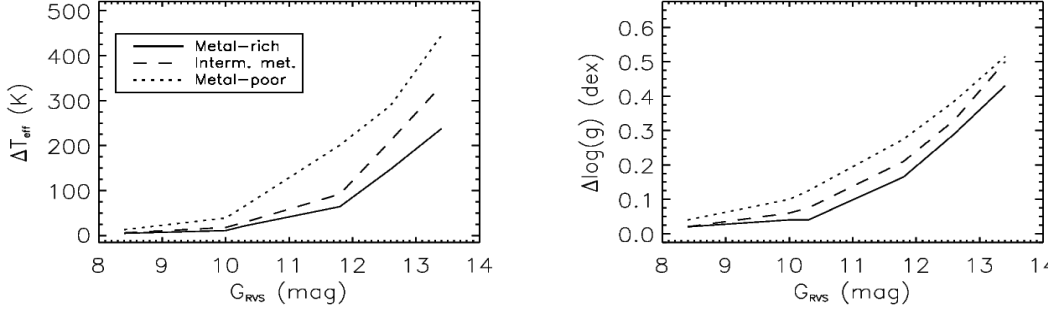
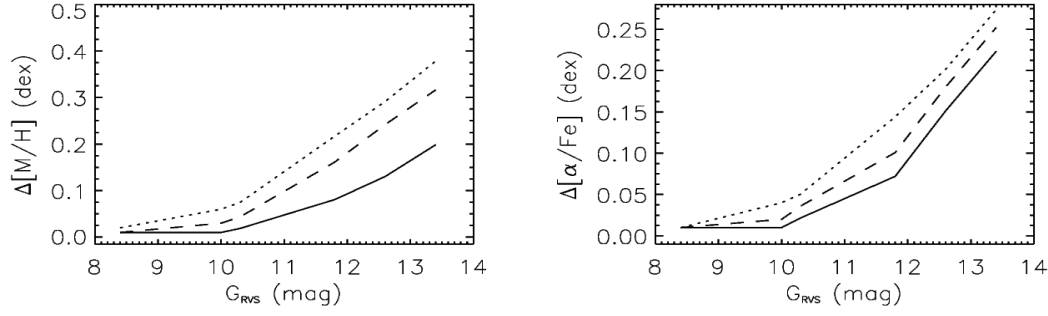
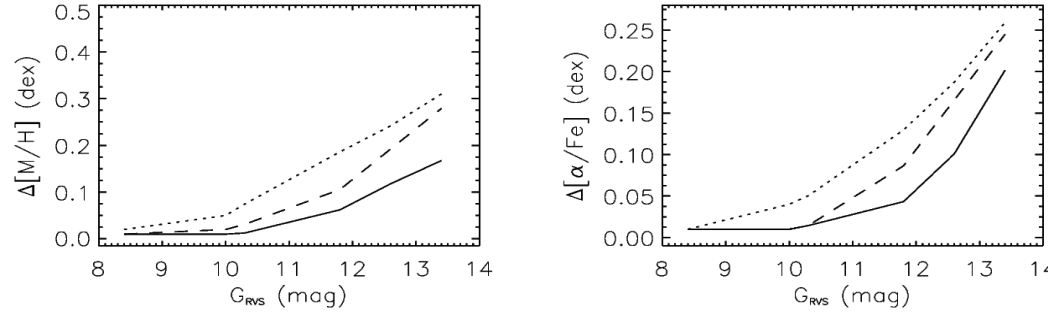


Fig. 17. Same as Fig. 16 but for the K-giant stars defined in Sect. 5.



the errors in T_{eff} , $\log(g)$ and $[M/H]$ on the three atmospheric parameters. First of all, the three right panels of Fig. 18, show how the errors in T_{eff} (right upper panel), $\log(g)$ (right middle panel) and $[M/H]$ (right bottom panel) depend on the stellar metallicity. In each case, two different curves are shown: the evolution of the 68% quantile for $G_{\text{RVS}}=10.3$ (red continuous line, $S/N=125$) and for $G_{\text{RVS}}=11.8$ (blue dashed line, $S/N=40$). As expected, the tendencies are more clearly appreciated at $G_{\text{RVS}}=11.8$ as the parametrization is more sensitive to loss (or gain) of information at lower S/N ratios.

First, it can be appreciated that the errors in the three parameters increase as the metallicity decreases, with a higher sensitivity for the metallicity error itself. In addition, the errors in T_{eff} increase as the metallicity decreases down to about

$[M/H]=-1.5$ dex. For lower stellar metallicities, the error in T_{eff} remains almost constant and practically independent of $[M/H]$. This is because for those metal-poor stars, the only useful temperature indicator that remains is the CaII triplet, which is present even at very low metallicities (see Fig. 2). A similar behaviour can be appreciated for the $\log(g)$ errors as a function of $[M/H]$ (right middle panel). However, in order to distinguish possible differences between FGK-type and early-type stars, Fig. 19 shows the evolution of the errors in $\log(g)$ and $[M/H]$ on the same two parameters, but separating FGK and early-type stars. The surface gravity error shows in fact a clear metallicity dependence (right upper panel of Fig. 19) down to $[M/H]=-1.5$ dex, and no dependence for lower metallicity stars.

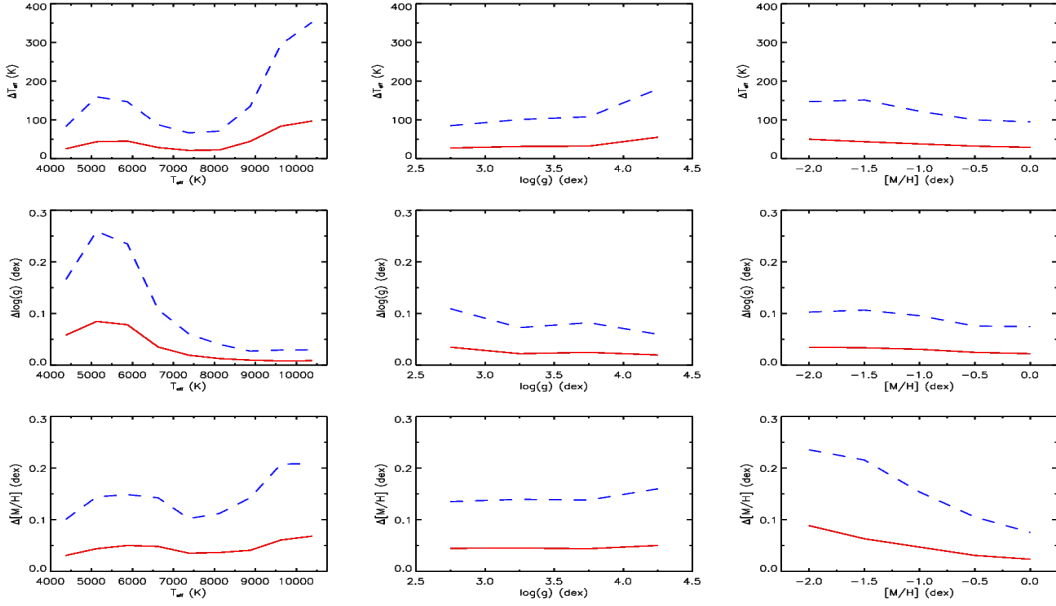


Fig. 18. Variation of the 68% quantile of the residuals for T_{eff} , $\log(g)$, $[M/H]$ for early- and late-type stars (end-of-mission *GSP-Spec* performances) as a function of the real atmospheric parameters for $G_{\text{RVS}}=10.3$ and 11.8 ($S/N = 125$ and 40) in solid red and dashed blue line, respectively. The adopted bins in T_{eff} , $\log(g)$, $[M/H]$ are 750 K, 0.5 dex and 0.5 dex, respectively.

Another important physical parameter influencing the parametrization performances is the effective temperature. This is illustrated in the three left panels of Fig. 18. In the range concerning FGK-type stars (T_{eff} approximately between 4 000 and 7 000 K), the behaviour of errors in T_{eff} , $\log(g)$ and $[M/H]$ shows a maximum around $\sim 5\,500$ K. From that point, the errors decrease in both directions, that is for lower and higher T_{eff} . In the first case (for lower T_{eff} stars), molecular signatures start to be visible in the spectra, being more abundant as the temperature decreases. Those molecular signatures are sensitive to both T_{eff} and $\log(g)$, as molecules formation is favoured for lower temperatures and higher gas pressure (and therefore $\log(g)$). In the second case (for stars with T_{eff} higher than about 6 000 K), the appearance of the hydrogen Paschen lines and their rapid change with T_{eff} brings a precious gravity indicator that reduces the errors in $\log(g)$ and breaks the T_{eff} - $\log(g)$ degeneracy (c.f. Sect. 5.2 and Sect. 5.3). As a consequence, the derivation of T_{eff} and $[M/H]$ are also improved for those hot stars.

Finally, the gravity influence on the stellar parametrization is illustrated by the middle panels of Fig. 18. The T_{eff} (upper middle panel) and the $[M/H]$ (bottom middle panel) derivation seem more difficult for dwarf stars than for giants, while the behaviour seems different for the $\log(g)$ estimation (central panel). In practice, the left panels of Fig. 19 showing the residuals of $\log(g)$ as a function of $\log(g)$ for FGK-type (upper left panel) and early-type stars (bottom left one), clarify the situation. For FGK stars, the gravity determination is in fact also more difficult for dwarfs than for giants, following the same tendency than the temperature and metallicity derivations. More generally, in both cases (FGK dwarfs and giants), the gravity is the more difficult parameter to estimate. This problem with the surface gravity is mostly caused by the lack of neutral and ionized lines of the same element in the RVS spectral domain. In any case, even for the lowest quality RVS spectra, the dichotomy between dwarf and giant stars will still be distinguishable.

In summary, the *Gaia* RVS data of FGK-type stars will allow accurate studies of the Galactic disc and halo populations. In particular, for stars with metallicity higher than around -0.5 dex, that will be the majority of the RVS survey, the metallicity and α -enrichment estimates will be very accurate, with typical errors smaller than 0.1 dex in $[\alpha/\text{Fe}]$ down to $G_{\text{RVS}}\sim 12.5$ (a few tens

of million of stars). In addition, K-giants will allow to perform Galactic studies up to distances of ~ 5 kpc (for $G_{\text{RVS}}=12$, and low extinction regions), or even ~ 12 kpc (for $G_{\text{RVS}}=13.5$).

5.2. Performances for early-type stars

Figure 20 shows the expected errors (defined again as the 68% quantile of the $\Delta\theta$ distributions) for A-type stars. As for FGK stars, three different curves are reported for each stellar parameter, illustrating the behaviour for metal-rich, metal-intermediate and metal-poor stars.

First of all, we can conclude that the parametrization of hot stars with $G_{\text{RVS}}\lesssim 12.5$, is expected to be very good (and actually excellent for the stellar surface gravity). As an example, the typical error in $[M/H]$ for hot metal-rich stars will be smaller than 0.1 dex down to that magnitude. In fact, this results from the pressure sensitivity of the Paschen lines that is a classical luminosity indicator for early-type stars, specially for $T_{\text{eff}}\gtrsim 9\,000$ K. This comes from the pressure dependence of the Stark effect. As a consequence, thanks to this important gravity indicator, hot stars show no dependence of the gravity estimation accuracy with any atmospheric parameter (c.f. Fig. 18 left middle panel, and Fig. 19 bottom panels). Only a small degradation with the S/N is detected. In contrast, both the estimation of the effective temperature and the metallicity are very sensitive to T_{eff} . In fact, the number of metallic lines drastically decreases for hot stars spectra.

Finally, even for faintest stars, the parameter accuracy is high enough to allow their classification into the main stellar classes (spectral subtypes, dwarf/subgiant/giant luminosity classes, with errors in $\log(g)$ lower than approximately 0.2 dex). The stellar metallicity is expected to be recovered with an error smaller than 0.8 dex for the faintest early-type stars (being smaller than 0.3 dex for A-type metal-rich stars). We recall that A-type dwarfs are bright stars that will allow to extend the RVS sounded volume up to distances of 5 Kpc from the Sun (for $G_{\text{RVS}}=14$).

5.3. Error correlations and parameter degeneracies

One important aspect to be considered in any parametrization exercise is the existence of error correlations. They not only in-

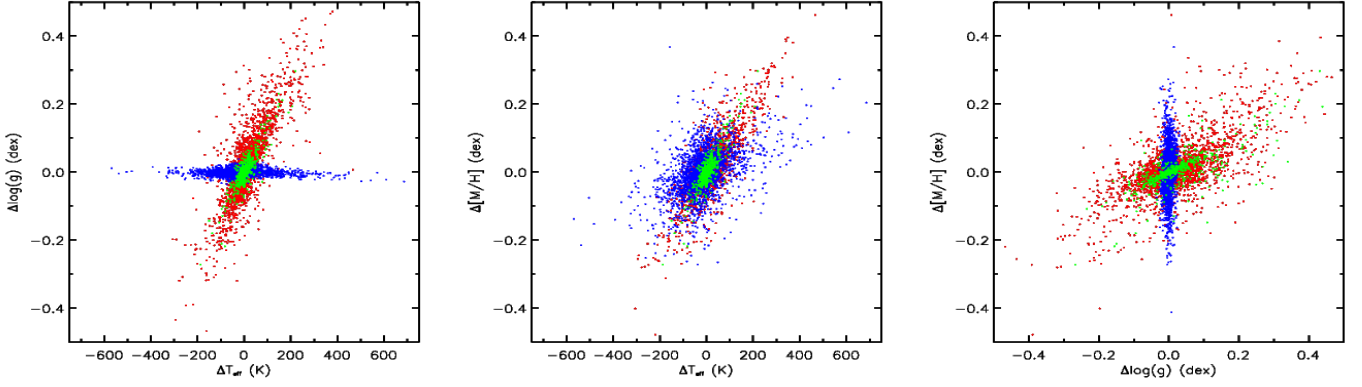


Fig. 21. Correlations between the residuals of the main atmospheric parameters for spectra at $G_{\text{RVS}}=10.3$ ($S/N=125$). Cool FGK-dwarf, cool K-giant, and hot BA-spectral type stars are plotted in red, green and blue, respectively. The main shape of these correlations does not change with G_{RVS} , only their amplitude varies.

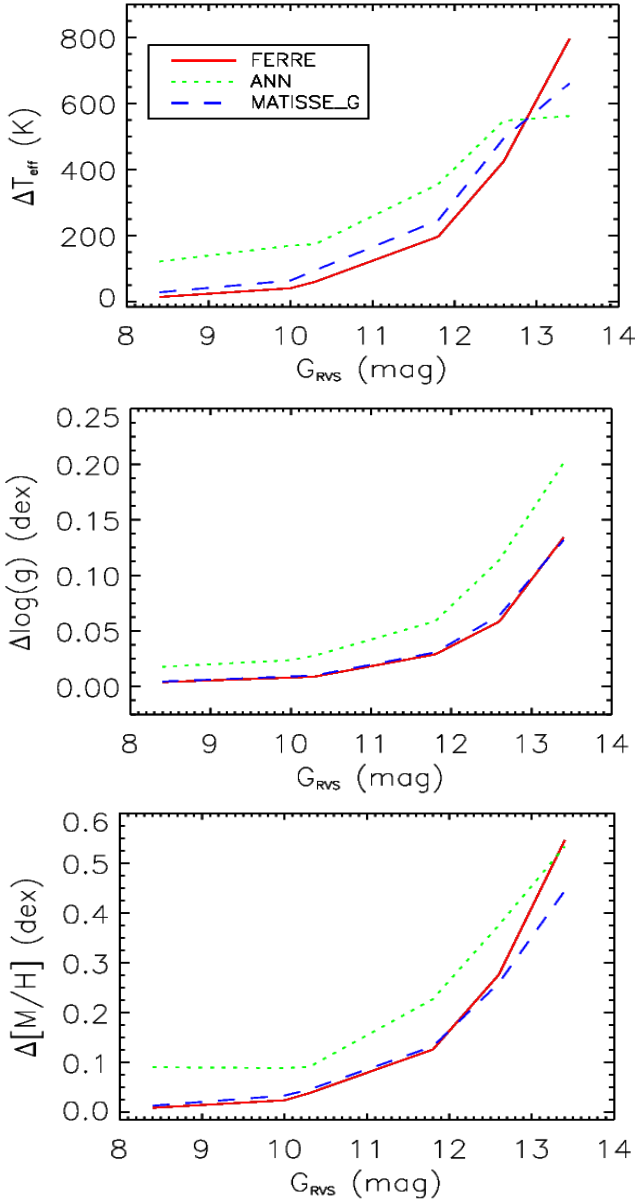


Fig. 10. Same as Fig. 9 but for the subsample of hot stars, defined by $T_{\text{eff}} > 8000$ K and $[M/H] \geq -1.0$ dex (1 457 spectra in total).

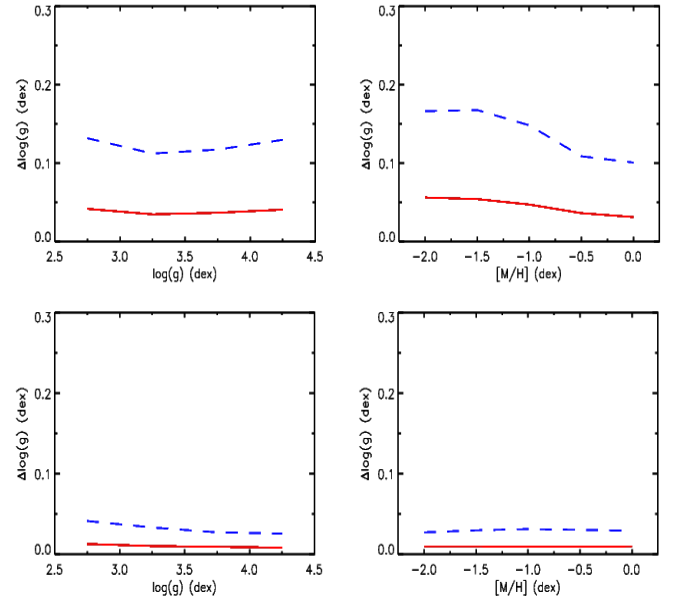


Fig. 19. Same as Fig. 18 but for the residuals in $\log(g)$, for cool-FGK and hot-BA stars separately (upper and lower panels, respectively).

form about the robustness of the results, but also on the possible physical sources of parameter degeneracies. Figure 21 shows the parameter error correlations at a given magnitude, $G_{\text{RVS}}=10.3$ ($S/N=125$), chosen for being the high quality regime, although with a high enough error amplitude for their analysis. Different colours have been assigned to FGK-dwarfs (red), K-giants (green) and BA-type stars (blue). First of all, a strong correlation is visible between the errors in surface gravity and effective temperature for the cool FGK-dwarfs. This comes from a known degeneracy between these two parameters (Kordopatis et al., 2011). On one hand, the wings of the CaII lines, carrying much of the information in the RVS domain, grow proportionally to $\log(g)^{1/3}$ for cool main sequence stars, but they also strongly depend on the T_{eff} . This implies that differences in the spectra with rather different parameters are very small, causing the error correlations seen in Fig. 21. This degeneracy is more important in the low metallicity regime, for which less metallic lines, carrying additional information on $\log(g)$, remain in the spectra. Moreover, as a consequence of the $T_{\text{eff}}-\log(g)$ degeneracy, the third atmospheric parameter, $[M/H]$, is also more difficult to constrain, showing also error correlations with the other two.

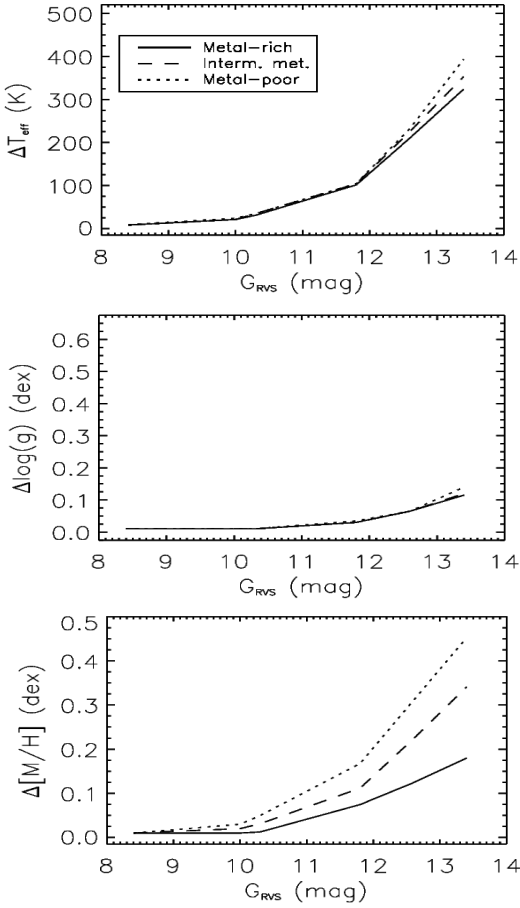


Fig. 20. Same as Fig. 16 but for the A-dwarf stars defined in Sect. 5.

On the other hand, K-giants do not suffer as much as dwarf stars from this $T_{\text{eff}}\text{-log}(g)$ error correlation, as shown by the green points of Fig. 21. This is because, as already discussed in Sect. 5.1, the parameterisation is easier for giant stars than for dwarfs, with more uncorrelated parameter variations.

Finally, BA-type stars (blue points in Fig. 21), thanks to the presence of a strong and sensitive surface gravity indicator (the Paschen lines), are not affected by $T_{\text{eff}}\text{-log}(g)$ or $[M/H]\text{-log}(g)$ degeneracies. This is illustrated by the flat behaviour of the $\log(g)$ errors as a function of the T_{eff} ones (left panel of Fig. 21), and the absence of a relation between the $[M/H]$ errors and the $\log(g)$ ones (right panel). Only a small correlation of the metallicity errors with the temperature ones (middle panel) seems to exist, in agreement with the discussions of Sect. 5.2.

6. Comparison with the expected performances from *Gaia* spectrophotometric data

In a study rather similar to the present one, Liu et al. (2012) reported the expected performances of stellar parameterisation from *Gaia* BP/RP spectrophotometry. Liu et al. (2012) analysed the results of different tested methods within the context of the DPAC/Working Group: *Global Stellar Parametrizer - Photometry (GSP-Phot)*. Some of the end-of-mission *GSP-Phot* expected performances have then been recently updated in Bailer-Jones et al. (2013, see their Tab. 4; see also Andrae et al., 2015, in preparation). The present section discusses the comparison between the expected end-of-mission parameterisation performances between RVS (*GSP-Spec*) and BP/RP (*GSP-*

Phot) data for stars brighter than $G_{\text{RVS}} \lesssim 15$. We recall that stars fainter than $G_{\text{RVS}} \sim 15$ will have only BP/RP based parameters. Moreover, it should also be pointed out that the present *GSP-Spec* analysis is performed for simulated RVS spectra that are not affected by any interstellar extinction, contrary to the Liu et al. (2012) results that rely on BP/RP spectra showing a large range of a priori unknown interstellar extinction. As a consequence, we will therefore assume in the following discussion that *GSP-Spec* is insensitive to interstellar extinction and we will only consider the Liu et al. (2012) results related to the smallest extinctions. Finally, although the tested random samples, the adopted statistical criteria and, the detailed performances for different types of stars and magnitudes are not exactly the same in our study and in the Liu et al. (2012) or the Bailer-Jones et al. (2013) ones, a rough quantification of the expected differences can still be performed. We point out that, in the following (as in the core of all these papers), the reported uncertainties in the recovered stellar atmospheric parameters refer to internal errors only, i.e. relative star-to-star uncertainties.

For the purpose of this *GSP-Phot* and *GSP-Spec* comparison, we adopted the relationship between the *G*-band (*Gaia* white light) and G_{RVS} magnitudes already presented in Tab. 2 and Fig. 4. It is then found that the G_{RVS} magnitude is brighter than the *G*-band one of about 0.3 mag for A-type stars, of 0.6 to 0.7 mag for F-type stars (with the magnitude range reporting the metallicity effect from metal-poor to metal-rich stars), of 0.8 to 1.0 mag for G-type stars and of 1.2 to 1.4 mag for the K spectral type. The variation between cool giants and cool dwarf stars is weak and has been neglected.

First, the study of Liu et al. (2012) reveals that the *GSP-Phot* stellar parameterisation is performed with almost the same efficiency as long as $G \lesssim 15$ and starts to degrade for fainter stars, only. This is also confirmed by the Tab.4 of Bailer-Jones et al. (2013) in which the performances at $G=9$ and $G=15$ are almost identical. On the contrary, the *GSP-Spec* parameterisation degrades earlier, for G_{RVS} fainter than ~ 11 or 12 mag, depending on the metallicity.

As pointed out in Sect.4.2, the $Q_{68\theta}$ and rms_{θ} statistical indicators can be assumed to be almost identical for low S/N RVS spectra. This allows us to compare our Tab. 5 and the Tab.4 of Bailer-Jones et al. (2013) to roughly deduce performance differences. Of course, this comparison can only show the tendencies suggested by tests on simulated data, neglecting external errors, mismatches between real data and models, parameterisation methods optimisation, etc... :

- Bright dwarf and giant A-type stars ($G_{\text{RVS}} \lesssim 12.5$) should probably be always better parametrized in T_{eff} , $\log(g)$ and $[M/H]$ from their RVS spectra. We recall that very good surface gravities and global metallicities (with an accuracy better than 0.1 dex) will be available for such type of stars from their *GSP-Spec* parameterisation. For A-stars fainter than $G_{\text{RVS}} \sim 12.5$, although $\log(g)$ and $[M/H]$ are still better estimated from their RVS spectra, the effective temperature derived from BP/RP data should be more accurate.
- The *GSP-Spec* effective temperature of F-type stars should probably be favoured for $G_{\text{RVS}} < 12.5$. Their *GSP-Spec* surface gravity and global metallicity should also be adopted as long as $G_{\text{RVS}} \lesssim 13$. Their accuracy should be better than 0.1 dex when $G_{\text{RVS}} < 12$.
- *GSP-Spec* stellar parameters of GK-spectral type stars should be adopted as long as $G_{\text{RVS}} \lesssim 12.5$.
- The global $[a/\text{Fe}]$ chemical index will be estimated from the *GSP-Spec* pipeline only for FGK-spectral type stars.

Uncertainties of the order of 0.1 dex (or even smaller) are expected as long as $G_{\text{RVS}} \lesssim 12\text{-}12.5$, depending on the metallicity.

In summary, it can be concluded that, for all the considered stellar types, the stars brighter than $G_{\text{RVS}} \sim 12.5$ ($S/N \sim 20$) will be very efficiently parametrized by the *GSP-Spec* pipeline, including good estimations of the $[\alpha/\text{Fe}]$ chemical index. From these stellar atmospheric parameters, individual chemical abundances (such as Fe, Ca, Ti, Si,...) will be derived with an expected uncertainty smaller than 0.1 dex for most of the RVS sample with about $G_{\text{RVS}} \lesssim 12$ ($S/N \gtrsim 35$), i.e. for a few million of targets. For faintest stars that are better parametrised from their BP/RP photometry, a T_{eff} input from *GSP-Phot* as an initial condition for *GSP-Spec* will allow the improvement of its final $\log(g)$, $[\text{M}/\text{H}]$ and $[\alpha/\text{Fe}]$ estimates. Such a *GSP-Phot*/*GSP-Spec* link is already implemented in the Apsis processing system developed by the CU8 and combined performance tests are being implemented.

Finally, we also stress that the spectral parametrization for extincted stars should be easier with the *GSP-Spec* pipeline since a T_{eff} -extinction degeneracy appears in the parametrisation of BP/RP low-resolution spectra with too large line-of-sight interstellar extinction (assuming that their brightness in the RVS band is not too faint to collect high enough S/N spectra). In those cases, a feedback from *GSP-Spec* to *GSP-Phot*, in a second iteration of the analysis cycle, will also improve the final parameters estimations.

7. Comparison with other spectroscopic surveys

A suite of ground-based vast stellar spectroscopic surveys mapping the Milky Way is revolutionizing the observational information about Galactic stellar populations. Their synergy with the *Gaia* mission relays not only on the sounded spatial volume, but also on their spectral resolution and covered wavelength domain. These two characteristics primarily determine their corresponding performances in the stellar parameters and chemical abundances estimation.

The Sloan Digital Sky Survey project, in its series of operations (SDSS I, II and III) has published about 250 000 spectra ($R=1800$) from the Sloan Extension for Galactic Understanding and Exploration (SEGUE; Yanny et al., 2009). SDSS spectra have provided only limited information on the structures revealed in the SDSS photometry, but they produced T_{eff} and $\log(g)$ estimates to 250 K and 0.5 cm/s^2 respectively, and $[\text{Fe}/\text{H}]$ abundances to 0.3 dex for stars with $14 < r < 19$ mag (Schlesinger et al., 2012). SEGUE data overlap the RVS targets only in the RVS fainter magnitudes domain. Due to the larger wavelength coverage of the SEGUE data, its T_{eff} estimations are generally better than the expected *GSP-Spec* ones. However, the higher RVS resolution should allow more precise measurements of $\log(g)$, and $[\text{M}/\text{H}]$.

The RAdial Velocity Experiment (RAVE; Steinmetz et al., 2006) is obtaining accurate radial velocities ($< 5 \text{ km/s}$) and global metallicities for $5 \cdot 10^5$ stars with $J < 12$ from spectra with $R=7500$. RAVE is also estimating the individual abundances of some elements for several thousand stars. This project, due to its rather bright magnitude limit, corresponding to about $G_{\text{RVS}}=12$ for solar type stars, is probing essentially the Galactic discs populations. In terms of parameter estimations, the RAVE internal errors at $\text{SNR}=10$ (about $G_{\text{RVS}}=12$) are of 350 K for T_{eff} , 0.5 dex for $\log(g)$ and 0.3 dex for $[\text{M}/\text{H}]$ for solar-type stars (cf. Kordopatis et al., 2013, Table 1). More generally, the *GSP-Spec*

performances should always be better than the RAVE ones, as expected from the RVS fainter magnitude limit and higher resolution.

More recently, the Large sky Area Multi-Object fiber Spectroscopic Telescope (LAMOST; Zhao et al., 2012) project has implemented a survey dedicated to Galactic exploration (LEGUE; Deng et al., 2012). The LEGUE survey plan includes spectra for 2.5 million stars brighter than $r < 19$ and an additional 5 million stars brighter than $r < 17$. The magnitude distribution depends on the telescope throughput and the survey resolution, much lower than the RVS one, is $R=1800$. Xiang et al. (2015) estimate the uncertainties of the LAMOST stellar parameter pipeline to be of about 150 K in T_{eff} , 0.25 dex in $\log(g)$ and 0.15 dex in $[\text{Fe}/\text{H}]$. On the other hand, for red giant stars, Liu et al. (2014) report typical errors in metallicity in the range 0.15 to 0.30 dex. On the other hand, similarly to the SEGUE survey, LEGUE data mainly overlap the RVS observations in the faint magnitudes domain, for which BP/RP data will also be available.

The results of the first low-resolution surveys revealed the key role of the stars chemical information to disentangle the Milky Way stellar population puzzle, motivating a new era of ground based high-resolution spectroscopic surveys. Three of them will be active from the ground during the period 2015-2019: The *Gaia*-ESO Survey (GES; Gilmore et al., 2012), the SDSS Apache Point Observatory Galactic Evolution Experiment (APOGEE; Eisenstein et al., 2011) and the Galactic Archaeology with AAO HERMES (GALAH; Zucker et al., 2012) survey. All these surveys, thanks to their larger wavelength coverage and resolution will provide more accurate parameters than *Gaia*/RVS for a subsample of stars. Nevertheless, only the GALAH survey, targeting about one million stars with $V < 14$, is expected to have an important overlap with the RVS. This overlap will correspond, in any case, to only less than one tenth of the RVS targets with $G_{\text{RVS}} < 13$. The GES survey is mainly targeting faint stars ($14 < V < 19$) thanks to the Very Large Telescope FLAMES/GIRAFFE facility ($R \sim 20\,000$) and it will primarily complement the *Gaia*/BPRP parameter estimations. In the RVS magnitude domain, only a small GES sample of 10^4 G-stars within 2 kpc of the Sun ($12 < V < 14.5$, corresponding to about $11 < G_{\text{RVS}} < 13.5$) is being observed with the FLAMES/UVES spectrograph ($R=40\,000$). Finally, the APOGEE survey, is preferentially targetting high extinction regions of the disc and the bulge in the range $8 < H < 13.8$. Although the magnitude coverage overlaps the RVS one, the APOGEE targeted fields are characterized by a high stellar crowding that limits the RVS observations. Therefore, APOGEE will mostly complement the RVS survey near the Galactic plane, rather than overlapping it.

In conclusion, the RVS based stellar parameters will provide precious information about the Galactic populations in the bright part of the *Gaia* volume, for a number of stars tens of times higher than what will be provided by currently on-going and planned spectroscopic surveys from the ground. Those surveys, specially those at high spectral resolution, will nevertheless be crucial for the *Gaia*/RVS parameters validation and to complement them with precise chemical abundances for a subsample of stars.

8. Conclusion

In this work, after having analysed the results of different independent methods, we have estimated the end-of-mission expected parametrization performances of the *Gaia* DPAC pipeline (*GSP-Spec*) in charge of the RVS stellar spectra atmo-

spheric parameters and chemical abundances derivation. The estimated accuracies, as a function of stellar types and magnitudes are summarized in Tab. 5 and in Fig 16 to 20.

The reported uncertainties in the recovered stellar atmospheric parameters refer to internal errors only, i.e. relative star-to-star uncertainties. Total errors will be, in many cases, dominated by external ones (partly caused by the possible synthetic spectra mismatches with respect to real observed ones) and they will be estimated from the analysis of real *Gaia* RVS spectra of benchmark reference stars, during a results validation phase. Nevertheless, the internal errors reported here permit to clearly identify, and quantify in detail, the enormous variety of science cases that will be obtained from the interpretation of pure *Gaia* data (without any need of references to external catalogues).

The *GSP-Spec* pipeline will be optimised in the light of the first analysed real RVS spectra over the next year. Increasingly improved versions of the Apsis *GSP-Spec* module are delivered at each operations cycle. *GSP-Spec* is expected to be running in operations cycle 4 in 2017, with a possible contribution from the third *Gaia* data release. The current *GSP-Spec* version, integrated in the general Apsis chain, already meets the tight requirements in processing speed (17 Mflops per source), needed to repeatedly treat tens of million of spectra.

Our tests, including first estimations of the impact caused by the on board detected stray light contamination, show that the contribution of the RVS based stellar parameters will be unique for stars with $G_{RVS} \lesssim 12.5$ (a few tens of million of stars). On the one hand, the *GSP-Spec* parameters will probably be more accurate than the majority of the parameters derived from the spectrophotometry in that magnitude range. This will allow, thanks to the use of the *Gaia* parallaxes, a better estimation of the stellar evolution phase and, as a consequence, of the isochrone based age estimations (for which the effective temperature accuracy is a dominant source of error). Accurate stellar ages will be one of the revolutions in Milky Way astrophysics that the *Gaia* mission will accomplish, and the RVS data will strongly contribute to it, sharpening our view of the Galactic history in a volume of very precise measurements (up to ~ 8 kpc from the Sun for K-giants and ~ 1 kpc for G-dwarfs).

On the other hand, accurate metallicity and chemical abundance measurements as the $[\alpha/\text{Fe}]$ content are today recognized as crucial information for the understanding of the highly complex evolution of Galactic stellar populations. As an example, the classical kinematically-based definitions of the thin and the thick disc populations blurred our comprehension of the Galactic disc substructure (c.f. Bovy et al., 2012; Recio-Blanco et al., 2014). The RVS chemical abundance estimations, with accuracies better than 0.1 dex, will therefore be a unique and precious sample of several million of stars for which many pieces of the Milky Way history puzzle will be available, with unprecedented precision and statistical relevance.

Acknowledgements. We thank the Centre National d'Etudes Spatiales (CNES, France) and the French CNRS/INSU for continuous support for the preparation of the *Gaia* mission. This work benefited from travel supports from the European Science Foundation through the GREAT Research Network Program. Part of the computations have been done on the 'Mesocentre SIGAMM' machine, hosted by the Observatoire de la Côte d'Azur. The first two authors would like to thank Naia for her (too) numerous (and efficient) attempts to postpone the revision of this paper. We warmly thank C.A.L. Bailer-Jones for his constructive remarks that helped to improve this article. We are also sincerely grateful to D. Katz for his help concerning the in-flight RVS characteristics.

References

Allende Prieto, C., Beers, T. C., Wilhelm, R., et al. 2006, *ApJ*, 636, 804

- Asplund, M., Grevesse, N., & Sauval, A. J. 2005, in *Astronomical Society of the Pacific Conference Series*, Vol. 336, *Cosmic Abundances as Records of Stellar Evolution and Nucleosynthesis*, ed. T. G. Barnes, III & F. N. Bash, 25
- Bailer-Jones, C. A. L., Andrae, R., Arcay, B., et al. 2013, *A&A*, 559, A74
- Barklem, P. S., Piskunov, N., & O'Mara, B. J. 2000, *A&AS*, 142, 467
- Bijaoui, A., Recio-Blanco, A., de Laverny, P., & Ordenovic, C. 2012, *Statistical Methodology*, 9, 55
- Bovy, J., Rix, H.-W., Liu, C., et al. 2012, *ApJ*, 753, 148
- Boyajian, T. S., McAlister, H. A., van Belle, G., et al. 2012, *ApJ*, 746, 101
- Bressan, A., Marigo, P., Girardi, L., et al. 2012, *MNRAS*, 427, 127
- Castelli, F. & Kurucz, R. L. 2003, in *IAU Symposium*, Vol. 210, *Modelling of Stellar Atmospheres*, ed. N. Piskunov, W. W. Weiss, & D. F. Gray, 20P
- de Bruijne, J. H. J. 2012, *Ap&SS*, 341, 31
- de Laverny, P., Recio-Blanco, A., Worley, C. C., et al. 2013, *The Messenger*, 153, 18
- de Laverny, P., Recio-Blanco, A., Worley, C. C., & Plez, B. 2012, *A&A*, 544, A126
- Deng, L.-C., Newberg, H. J., Liu, C., et al. 2012, *Research in Astronomy and Astrophysics*, 12, 735
- Eisenstein, D. J., Weinberg, D. H., Agol, E., et al. 2011, *AJ*, 142, 72
- Fleitas, J., Davidson, M., Katz, D., Els, S., & de Bruijne, J. 2015, in *ESA/DPAC Note: GAIA-CO-TN-ESAC-JMF-012-01-00*
- Gilmore, G., Randich, S., Asplund, M., et al. 2012, *The Messenger*, 147, 25
- Grevesse, N. & Sauval, A. J. 1998, *Space Sci. Rev.*, 85, 161
- Guiglion, G., Recio-Blanco, A., & de Laverny, P. 2014, in *IAU Symposium*, Vol. 298, *IAU Symposium*, ed. S. Feltzing, G. Zhao, N. A. Walton, & P. Whitelock, 408–408
- Jordi, C., Gebran, M., Carrasco, J. M., et al. 2010, *A&A*, 523, A48
- Koesterke, L. 2009, in *American Institute of Physics Conference Series*, Vol. 1171, *American Institute of Physics Conference Series*, ed. I. Hubeny, J. M. Stone, K. MacGregor, & K. Werner, 73–84
- Koesterke, L., Allende Prieto, C., & Lambert, D. L. 2008, *ApJ*, 680, 764
- Kordopatis, G., Gilmore, G., Steinmetz, M., et al. 2013, *AJ*, 146, 134
- Kordopatis, G., Recio-Blanco, A., de Laverny, P., et al. 2011, *A&A*, 535, A106
- Liu, C., Bailer-Jones, C. A. L., Sordo, R., et al. 2012, *MNRAS*, 426, 2463
- Liu, C., Deng, L.-C., Carlin, J. L., et al. 2014, *ApJ*, 790, 110
- Manteiga, M., Ordóñez, D., Dafonte, C., & Arcay, B. 2010, *PASP*, 122, 608
- Ramírez, I. & Meléndez, J. 2005, *ApJ*, 626, 465
- Recio-Blanco, A., Bijaoui, A., & de Laverny, P. 2006, *MNRAS*, 370, 141
- Recio-Blanco, A., de Laverny, P., Kordopatis, G., et al. 2014, *A&A*, 567, A5
- Schlesinger, K. J., Johnson, J. A., Rockosi, C. M., et al. 2012, *ApJ*, 761, 160
- Steinmetz, M., Zwitter, T., Siebert, A., et al. 2006, *AJ*, 132, 1645
- Worley, C. C., de Laverny, P., Recio-Blanco, A., et al. 2012, *A&A*, 542, A48
- Xiang, M. S., Liu, X. W., Yuan, H. B., et al. 2015, *MNRAS*, 448, 822
- Yanny, B., Rockosi, C., Newberg, H. J., et al. 2009, *AJ*, 137, 4377
- Zhao, G., Zhao, Y., Chu, Y., Jing, Y., & Deng, L. 2012, *ArXiv e-prints*
- Zucker, D. B., de Silva, G., Freeman, K., Bland-Hawthorn, J., & Hermes Team. 2012, in *Astronomical Society of the Pacific Conference Series*, Vol. 458, *Galactic Archaeology: Near-Field Cosmology and the Formation of the Milky Way*, ed. W. Aoki, M. Ishigaki, T. Suda, T. Tsujimoto, & N. Arimoto, 421